Exploring the Design of Multiferroic Materials by Nanocrystal Building Block Approach

by

Penghui Yin

A thesis
presented to the University of Waterloo
in fulfillment of the
thesis requirement for the degree of
Master of Science
in
Chemistry-Nanotechnology

Waterloo, Ontario, Canada, 2015

Author's Declaration

I hereby declare that I am the sole author of this thesis. This is a true copy of the thesis, including any required final revisions, as accepted by my examiners.

I understand that my thesis maybe made electronically available to the public.

Abstract

Multiferroic materials have been extensively studied as they exhibit both magnetic and electric properties simultaneously, and could be potential candidate materials for the new generation of magnetoelectric (ME) devices. Perovskite materials with room-temperature ferroelectric ordering and simple crystal structure have emerged as favorable building blocks for developing multiferroic devices. In this work, we investigated different approaches to introducing magnetic properties into ferroelectric $BaTiO_3$ and $PbTiO_3$ nanostructures synthesized by hydrothermal method. Specifically, we investigated doping of perovskite nanostructures with magnetic centers as an intrinsic approach, and the formation of nanocomposite with ferrimagnetic spinel $Co_{0.6}Fe_{2.4}O_4$ nanocrystals as an extrinsic approach to multiferroic nanostructures with different morphologies. Investigation of morphology, crystal structure, and magnetic properties of nanoscale perovskite materials and their heterostructures shows promising results towards developing materials which exhibit room-temperature multiferroic properties.

Mn-doped $BaTiO_3$ nanoparticles (NPs) were synthesized with different size and doping concentrations. Small particle size and high doping concentration favor the crystal phase transformation from tetragonal to cubic crystal structure. Mn-doped $BaTiO_3$ NPs prepared in ethanol with an average size of ca. 6.4 nm show evidence of tetragonal crystal structure with doping concentration up to 10%. UV-visible absorption spectrum of the colloidal sample indicates the existence of Mn^{3+} ions in $BaTiO_3$ lattice which is further confirmed by Mn L-edge X-ray absorption spectrum. Additional magnetic and magneto-optical properties measurements could shed light on the single-phase multiferroic nanomaterials.

Multiferroic composites were attempted by incorporating ferroelectric $BaTiO_3$ and ferrimagnetic $Co_{0.6}Fe_{2.4}O_4$ NPs through impregnation or spin coating. Multi-domain structure is

observed in high resolution transmission electron microscopy (HRTEM) images of the nanocomposite consisting of $BaTiO_3$ and $Co_{0.6}Fe_{2.4}O_4$ nanostructures. X-ray diffraction and Raman spectroscopy measurements indicate the existence of tetragonality in both type of composites after annealing at 373 K. In addition, magnetic measurements suggest that the composites have enhanced coercivity compared to ferrimagnetic component alone. Transparent multiferroic multi-layer structure was obtained by spin-coating transparent $PbTiO_3$ thin films with $Co_{0.6}Fe_{2.4}O_4$ nanocrystals. This structure provides an opportunity to study the ME coupling between two building blocks with different magneto-optical spectroscopies.

Acknowledgements

First, I would like to express my sincere gratitude to my supervisor Dr. Pavle Radovanovic for his invaluable support throughout the project. His guidance and enthusiasm towards science encouraged me to face many difficulties I encountered and become a better researcher.

I would like to thank my committee members, Dr. Holger Kleinke and Dr. Eric Prouzet, for their time and insightful advice during my study. I also thank Dr. Dan Thomas for being on my examining committee for my thesis defence and giving me suggestions on my work.

I would like to acknowledge Dr. Carmen Andrei at the Brockhouse Institute for Materials Research for her assistance in TEM image collection. I also thank Peng Peng for his aid in Raman spectroscopy measurement in Giga-to-Nanoelectronics Center at the University of Waterloo. I would like to acknowledge the Kleinke lab, and especially Quansheng Guo, at the University of Waterloo for their help with XRD pattern collection.

I would also like to thank my past and present fellow group members for their assistance and encouragement. I had the pleasure of working closely with current group members Vahid, Paul, Manu, Natalie, Hanbing, and Enas. In particular, I would like to thank Manu for his help in SEM image collection as well as teaching me the principles and data analysis of XAS. I also acknowledge past group member Lisa for helping me to get off a good start in the lab, her suggestions were very helpful.

Last but not least, I am grateful to my parents for their understanding and support. Their love gives me the energy to reach my goals.

Contents

Author's Declaration ii

Abstract iii

Acknowledgements v

Contents vi

List of Figures ix

List of Abbreviations xiii

Chapter 1 Introduction 1

1.1 Ferroelectric Materials 1

1.2 Ferro/ferrimagnetic Materials 5

1.3 Multiferroics 9

1.3.1 Single-phase Multiferroics 10

1.3.1.1 Introducing Ferroelectric Ordering into Magnetic Materials 11

1.3.1.2 Introducing Magnetic Ordering into Ferroelectric Materials 13

1.3.2 Multiferroic Composites 15

1.4 Motivations and Scope of the Thesis 18

Chapter 2 Experimental Section 20

2.1 Materials 20

2.2 Synthesis and Sample Preparation 20

2.2.1 Synthesis of $BaTiO_3$ NPs 20

2.2.2 Synthesis of Mn-doped $BaTiO_3$ NPs 21

2.2.3 Synthesis of $BaTiO_3$ NPs with Small Size 21

2.2.4 Synthesis of $CoFe_2O_4$ NPs 22

2.2.5 Synthesis of $Co_{0.6}Fe_{2.4}O_4$ NCs 22

2.2.6 Synthesis of $BaTiO_3/Co_{0.6}Fe_{2.4}O_4$ Composite by Impregnation Method 23

2.2.7 Synthesis of $BaTiO_3/Co_{0.6}Fe_{2.4}O_4$ Multilayer Films by Spin-coating Method 23

2.2.8 Synthesis of $PbTiO_3/Co_{0.6}Fe_{2.4}O_4$ Multilayer Films by Spin-coating Method 23

2.2.9 Synthesis of $PbTiO_3$ Nanoribbons 24

2.3 Characterization Techniques 24

2.3.1 Powder X-ray Diffraction 24

2.3.2 UV-Visible (UV-vis) Absorption Spectroscopy 25

2.3.3 Raman Spectroscopy 25

2.3.4 Electron Microscopy 26

2.3.5 Magnetization Measurement 27

2.3.6 X-ray Absorption Spectroscopy 27

Chapter 3 Study of Mn-doped $BaTiO_3$ Nanoparticles 30

3.1 Structures Determined by X-ray Diffraction 30

3.2 Morphology 31

3.3 Phase Transition Determined by Raman Spectroscopy 34

3.4 Effect of Dopant Ions in Ethanol-Synthesized Mn-doped $BaTiO_3$ 36

3.5 UV-visible Absorption Spectrum 38

3.6 X-ray Absorption Spectrum 40

Chapter 4 Synthesis of $BaTiO_3/CoFe_2O_4$ Composites 42

4.1 $BaTiO_3$ Building Blocks 42

4.2 $Co_{0.6}Fe_{2.4}O_4$ Building Block 45

4.3 CFO-BTO Composites 50

Chapter 5 Synthesis of $Co_{0.6}Fe_{2.4}O_4$-$PbTiO_3$ Composite 56

5.1 $PbTiO_3$ Thin Films 56

5.2 $Co_{0.6}Fe_{2.4}O_4$-$PbTiO_3$ Multilayer Structure 60

5.3 Alternative $PbTiO_3$ Nanostructure 63

Chapter 6 Conclusions and Future Work 66

6.1 Mn-doped $BaTiO_3$ 66

6.2 $Co_{0.6}Fe_{2.4}O_4$-$BaTiO_3$ Composite 67

6.3 $Co_{0.6}Fe_{2.4}O_4$-$PbTiO_3$ Composite 68

Appendix 69

References 72

List of Figures

Figure 1-1: Unit cell structures of (a) cubic $BaTiO_3$ (space group *Pm3m*) and (b) tetragonal $BaTiO_3$ (space group *P4mm*). Color code: Ba, green; O, red; Ti, blue. The positions of the asymmetric O atoms in the tetragonal phase are indicated as O_I and O_{II}.[5] 2

Figure 1-2: Double well potential energy of Ti^{4+} ions as a function of the position between two O^{2-} ions.[7] 3

Figure 1-3: Hysteresis loop that includes the initial magnetization curve. Also shown are coercivity H_c and remanent magnetic flux density B_r. A hysteresis loop can be obtained by plotting magnetic field density B vs. applied magnetic field intensity H.[27] 6

Figure 1-4: Schematic representation of the inverse spinel structure of $CoFe_2O_4$ with tetrahedral (A) and octahedral (B) sites. Pink spheres represent metal ions (half of Fe^{3+} ions) in A sites and green spheres represent metal ions (half of Fe^{3+} and all of Co^{2+} ions) in B sites. O atoms are located at the vertices of each polyhedron which are not shown in this figure. 8

Figure 1-5: Interactions in multiferroics. Primary ferroic orderings, ferroelectricity (P), ferromagnetism (M), and ferroelasticity (ε), can be switched by their conjugate electric (E), magnetic (H), and stress (σ) fields, respectively[42] 9

Figure 1-6: $TbMnO_3$ crystal structure under room temperature. The orange arrow denotes the magnetic moment of Mn^{3+} below T_N[50]. 12

Figure 1-7: Representation of magnetic polarons. A donor electron in its hydrogenic orbit couples with its spin antiparallel to impurities with a 3d shell that is half-full or more than half-full. The figure is drawn for x (concentration of magnetic cations) = 0.1, γ = 12. Cation sites are represented by small circles. Oxygen is not shown; the unoccupied oxygen sites are represented by squares.[58] 15

Figure 1-8: (a) Epitaxial alignment of a spinel (top left) and a perovskite (top right) on a perovskite substrate (bottom). (b) Schematic illustration of a self-assembled nanostructured thin film formed on the substrate.[62] 16

Figure 1-9: Illustration of experimental geometry and (deformed) shapes of CFO nanopillar's unit cells within apical polarization vector of the BTO environment ±Px,y.[70] 18

Figure 2-1: The d orbital splitting in cubic, tetrahedral and octahedral crystal field[72] 25

Figure 2-2: scheme of sample preparation of films from colloidal $Co_{0.6}Fe_{2.4}O_6$ for magnetization measurements. 27

Figure 3-1: (a) Representative XRD patterns of Mn-doped $BaTiO_3$ samples synthesized in water, ethanol, and benzyl alcohol. The vertical black and red lines correspond to the XRD patterns of bulk cubic (JCPDS no. 31-0174) and tetragonal (JCPDS no. 05-0626) $BaTiO_3$, respectively. (b) Enlarged XRD pattern around cubic (200) peak and tetragonal (200) and (002) peaks..... 30
Figure 3-2: Representative TEM images of Mn-doped $BaTiO_3$ synthesized in (a) water, (b) ethanol, and (c) benzyl alcohol. The insets: High resolution TEM images showing measured lattice spacing. 33
Figure 3-3: STEM image of a single Mn-doped $BaTiO_3$ nanoparticle with the EDX line scan profile on top of it. The inset shows the corresponding element of lines in line scan profile. 34
Figure 3-4: Raman spectra of Mn-doped $BaTiO_3$ NPs synthesized in different solvents and commercial powder (red trace) as comparison. The assignments of the Raman modes are indicated at the top of the figure. Inset: enlarged spectra of in the E(TO+LO), B_1 region (ca. 300 cm^{-1}) for NPs prepared in water (black), ethanol (blue), and benzyl alcohol (green). 35
Figure 3-5: (a) XRD patterns of Mn-doped $BaTiO_3$ samples synthesized in ethanol with different starting Mn/Ti ratio. The vertical lines correspond to the XRD patterns of bulk cubic (black) and tetragonal (red) $BaTiO_3$. (b) Enlarged XRD pattern around cubic (200) peak and tetragonal (200) and (002) peaks. 37
Figure 3-6: Raman spectra of Mn-doped $BaTiO_3$ NPs prepared in ethanol with different starting Mn/Ti molar ratios of 5%, 10% and 15%. 38
Figure 3-7: Typical UV-visible absorption spectrum (red) of colloidal Mn-doped $BaTiO_3$ NPs. The spectrum of concentrated samples (black) reveal the ligand field transition of Mn^{3+}. Inset: A schematic representation of the ligand field energy state splitting of Mn^{3+} in distorted octahedral site. 39
Figure 3-8: (a) Mn L-edge XAS spectrum of 10% Mn-doped $BaTiO_3$. (b) Linear combination of calculated XAS spectrum for Mn^{2+} (c) and Mn^{3+} (d). 41
Figure 4-1: (a) XRD patterns of BTO1 and BTO2. The vertical lines correspond to XRD patterns of bulk cubic (black) and tetragonal (red) $BaTiO_3$. (b) Enlarged XRD pattern around cubic (200) peak (black line) and tetragonal (200) and (002) peaks (red lines). 43
Figure 4-2: (a) Representative overview TEM image of BTO2 sample. Inset: SAED image of the aggregate shown in the image. (b) HRTEM image of BTO2 sample. Inset: HRTEM image of separated NPs. 44

Figure 4-3: Raman spectra of BTO1, BTO2 samples and commercial bulk $BaTiO_3$. Inset: Enlarged spectrum around ca. 300 cm^{-1} region. 45
Figure 4-4: Representative XRD pattern of CFO sample. The vertical line corresponds to the XRD pattern of bulk $CoFe_2O_4$ (JCPDS no. 22-1086)..... 46
Figure 4-5: (a) Representative TEM image of CFO sample. Inset: HRTEM image of a single nanocrystal. (b) Size distribution histogram of CFO NCs. 47
Figure 4-6: Raman spectrum of synthesized CFO sample..... 48
Figure 4-7: Representative UV-visible absorption spectrum of CFO NCs. (Note that the parentheses denote tetrahedral coordination and square brackets denote octahedral coordination.) Inset: Enlarged spectrum at 400-540 nm region. 49
Figure 4-8: Magnetic hysteresis loop of synthesized CFO sample measured at room temperature. 50
Figure 4-9: XRD patterns of composites obtained by impregnation (a) and spin coating (b). The dash lines correspond to XRD patterns of respective building blocks. The vertical lines in (c) represent the XRD pattern of bulk $BaTiO_3$ (red) and $CoFe_2O_4$ (black). 51
Figure 4-10: TEM images of the composites obtained by impregnation (a) and spin coating (d). (b) and (c) HRTEM images from different spots on image(a). (e) HRTEM image of CFO-BTO2 thin film sample..... 53
Figure 4-11: Raman spectra of the composite prepared with impregnation (a) and spin coating (b) method. The traces with dash line are Raman spectra of corresponding build blocks. 54
Figure 4-12: Magnetic hysteresis loops collected under different temperature of the composites prepared by impregnation (a) and spin coating (b). 55
Figure 5- 1: XRD patterns of as-synthesized NPs with (black) and without annealing (purple) and annealed $PbTiO_3$ thin film (blue). Inset: Enlarged XRD pattern of annealed thin film at the region around tetragonal $PbTiO_3$ (101) and (110) diffraction peaks. The vertical lines represent of bulk tetragonal (red, JCPDS no. 06-0452) and cubic (black, JCPDS no. 40-0099) $PbTiO_3$. 57
Figure 5- 2: Low (a) and high (b) magnification SEM images of anneled $PbTiO_3$ thin film. 58
Figure 5- 3:Raman spectra of the annealed powder (black) and thin film(blue). The red dash line is Raman spectra of the thin film without annealing. The assignments of the Raman modes are indicated at the top of the graph..... 59

Figure 5- 4: UV-visible absorption spectrum of obtained $PbTiO_3$ thin film. Inset: Photograph of the thin film. 60
Figure 5- 5: Low magnification (a) and high resolution (b) TEM images of obtained $PbTiO_3$ thin film. 61
Figure 5- 6: Raman spectrum of CFO-PTO thin film. 61
Figure 5- 7:UV-visible absorption spectrum of CFO-PTO thin film (black) and PbTiO3 thin film as comparison (red dash line). 62
Figure 5- 8: XRD patterns of samples synthesized with 10 mmol (black) and 20 mmol (blue) NaOH. The red vertical line at the bottom represents XRD pattern of bulk tetragonal $PbTiO_3$. 63
Figure 5- 9: Low (a) and high (inset) magnification SEM images of the samples synthesized with 10 mmol NaOH. SEM (b) and TEM (c) images of the sample synthesized with 20 mmol NaOH. (c) Inset: HRTEM image of a single nanoribbon. 65
Figure A1: Particle size histogram of 10% Mn-doped $BaTiO_3$ synthesized in benzyl alcohol (a) and ethanol (b). 69
Figure A2:Fe (a) and Ti (b) $L_{3,2}$-edge XANES (top) and XMCD (bottom) in composite of $CoFe_2O_4$ and $BaTiO_3$ 70
Figure A3: STEM image of the fragment of CFO-PTO thin film with corresponding EDX elemental maps of Co, Fe, Pb, Ti, and O in STEM…… ……71

List of Abbreviations

T_C	Curie temperature
DMSOs	Diluted magnetic semiconductor oxides
EDX	Energy dispersive X-ray spectroscopy
HR-TEM	High resolution transmission electron microscopy
MCD	Magnetic circular dichroism
ME	Magnetoelectric
NCs	Nanocrystals
NPs	Nanoparticles
PPMS	Physical property measurement system
SEM	Scanning electron microscopy
STEM	Scanning transmission electron microscopy
TEM	Transmission electron microscopy
TOPO	Trioctylphosphine oxide
UV-vis	Ultraviolet-visible
XAS	X-ray absorption spectroscopy
XMCD	X-ray magnetic circular dichroism
XRD	X-ray diffraction

Chapter 1 Introduction

1.1 Ferroelectric Materials

Ferroelectric materials have spontaneous polarization whose direction and magnitude can be tuned by external electric field.[1] However, when temperature increases beyond certain value (Curie Temperature, T_C), the ferroelectric will undergo the structural transformation to the so-called high temperature phase which behaves like a normal dielectric material.[2] The ferroelectric effect was first observed by Valasek in 1921 in the Rochelle salt, which has the formula of $KNaC_4H_4O_6 \cdot 4H_2O$.[3] The fundamental studies on the origin of the ferroelectricity in the Rochelle salt are very difficult because of its complex crystal structure with large number of atoms in the unit cell. After several materials with perovskite structure found to be ferroelectric, the perovskites became a hot spot in this field due to its relatively simple crystal structure.

$BaTiO_3$ and $PbTiO_3$ are well understood ferroelectric perovskites at room temperature. Barium titanate can exist in four different phases depending on the temperature: the paraelectric cubic phase, the ferroelectric tetragonal phase, the orthorhombic phase, and the rhombohedral phase.[4] Paraelectric cubic perovskite $BaTiO_3$ is stable at temperatures above 393 K, while at temperatures between 273 to 393 K, the bulk barium titanate adopts the tetragonal phase which is ferroelectric. The difference between cubic and tetragonal phases is shown in Figure 1-1. In tetragonal phase, Ti^{4+} ion shifts away from the center of the TiO_6 octahedron along one of the <001> direction, which propagates thorough the whole lattice resulting in the net polarization along <001>.[5] $PbTiO_3$ undergoes the similar structural transformation from tetragonal phase to cubic phase with much higher transition temperature (T_C = 763 K). Under 763 K, the tetragonal $PbTiO_3$ has the net polarization along <001> direction.[6]

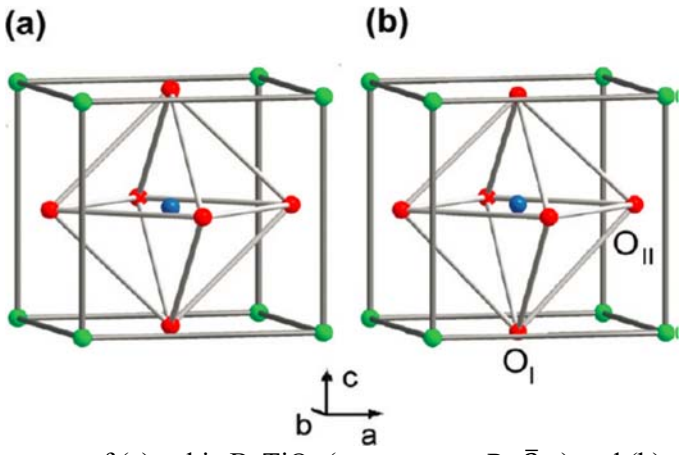

Figure 1-1: Unit cell structures of (a) cubic $BaTiO_3$ (space group $Pm\bar{3}m$) and (b) tetragonal $BaTiO_3$ (space group $P4mm$). Color code: Ba, green; O, red; Ti, blue. The positions of the asymmetric O atoms in the tetragonal phase are indicated as O_I and O_{II}.[5]

Normally, a lattice of opposite charges is inherently unstable. Ionic materials are stable because of the short-range repulsions between electron clouds of the adjacent ions. This short-range repulsion favors the crystallographic symmetric structure which is non-ferroelectric. In ferroelectric materials, in order to stabilize the distorted structure, there should be an additional bonding to balance short-range repulsion between adjacent ions.[7] Cohen in 1992 calculated the electronic structure of $BaTiO_3$ using first principle and found an overlap of the Ti 3d partial densities of states with the O 2p valence bands.[8] It is suggested that, at low temperature, Ti 3d- O 2p hybridization is crucial for stabilizing the tetragonal ferroelectric phase. At temperature beyond T_C, the short-range repulsion force becomes dominant and the material adopts the symmetric cubic structure. In the case of $PbTiO_3$, in addition to Ti 3d-O 2p hybridization, there is another overlap between the Pb 6s and O 2p orbitals.[9] This allows distorted tetragonal phase to be stabilized at a much higher temperature compared to $BaTiO_3$. The additional Pb 6s-O 2p overlap gives a higher c/a ratio of 1.06 and net spontaneous polarization of 75 $\mu C/cm^2$ compared to c/a ratio of 1.01 and polarization of 26 $\mu C/cm^2$ of $BaTiO_3$.[10,11]

Currently, there are two phenomenological models which describe the phase transition of the ferroelectric perovskite. In one model, the potential energy (U) of Ti^{4+} ions as a function of the distance (R) between oxygen ions has the "double well" shape as shown in Figure 1-2. The Ti^{4+} ions can lower its energy by shifting away from the center of the octahedron along one of the <111> direction. From the point of view of crystal structure, at low temperature, Ti^{4+} ions shift along one of the <111> direction which leads to the rhombohedral phase. As temperature increases, the orthorhombic structure is adopted since Ti^{4+} ions displace over two directions along the space diagonal. Ti^{4+} ions disorder along four directions resulting in the tetragonal symmetry. Eventually, when the temperature is higher than T_C, it adopts the cubic phase with eight possible directions for the Ti^{4+} ions displacement.[12]

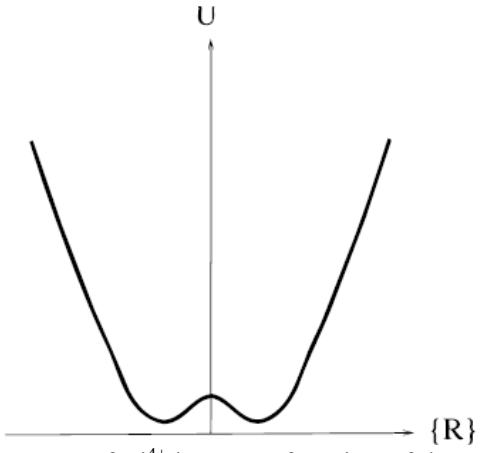

Figure 1-2: Double well potential energy of Ti^{4+} ions as a function of the position between two O^{2-} ions.[7]

In the other model, at high temperature, the so called "soft-model" phonon will push the Ti^{4+} ions back to the symmetric sites in the octahedron.[13] While, the "soft model" phonon will get much weaker when the temperature is reduced towards T_C. As a result, the distorted tetragonal structure is stabilized over cubic structure.

The ferroelectric properties are not only affected by the temperature-dependent phase transformation, but also affected by the grain size of the perovskite nanoparticles (NPs). In the

case of $BaTiO_3$, the ratio of the lattice constant in c direction to that in a direction (c/a ratio) will decrease with decreasing particle size, which makes the ferroelectric phase become unstable when the grain size is reduced below the critical value.[14] However, a wide range of critical size values have been reported both in theoretical calculations and experimental data (from 40 nm[15] to 4.2 nm[16]). Li and Shih found that clustering also has an effect on phase transition.[17] The NPs which would be cubic as free standing particles might attain the tetragonal structure when clustered. However, the transition temperature from tetragonal to cubic phase is not sensitive to particle size for both separate particles and clusters. The experimental band gap energy of $BaTiO_3$ is 3.2 eV.[18] Adireddy *et al.*[19] synthesized monodisperse cube-like $BaTiO_3$ NPs with particle sizes of ca. 20 nm. They claim that those NPs having cubic phase with local tetragonal distortion could be used as ferroelectric building blocks. Polking *et al.*[20] studied ferroelectric properties of individual $BaTiO_3$ NPs synthesized using the above solution method. During the electric measurement, they observed electric hysteresis for those NPs at room temperature. Additionally, atomic-resolution mapping showed titanium displacement among individual single-crystalline NPs. The piezoresponse force microscopy studies indicated that the room-temperature ferroelectric polarization disappeared when the particle size was decreased to 5 nm.

$PbTiO_3$ NPs behave similarly to $BaTiO_3$ regarding the size effect upon ferroelectric properties. Although, there is no consensus in the literature in terms of the critical size under which the tetragonal phase cannot be stabilized, several literature reports suggested that the $PbTiO_3$ NPs clearly keep tetragonal phase under room temperature at least with the size of 22 nm.[21,22,23] Ishikawa *et al.*[22] reported they observed a well-defined soft-mode line in Raman spectrum which indicates the tetragonal phase at room temperature for 22 nm particles. In addition, based on their experimental results, they derived empirical expression of the relationship between the phase

transition temperature and particle size. By using that expression, they further extrapolated the critical size to be 13.8 nm. From the X-ray diffraction (XRD) measurement, Zhong *et al.*[23] found that the c/a ratio of $PbTiO_3$ only changes from 1.065 for 200 nm particles to 1.059 for 22 nm NPs. Analysing their data in the similar way as Ishikawa *et al.*, the critical size is calculated to be 9.1 nm. With the development of new synthetic method, $PbTiO_3$ with small crystallite size was able to be obtained and investigated. In the study done by Keijser *et al.*[24], the c/a ratio of the $PbTiO_3$ crystallite was found to approach 1 when the size decreases close to ca. 5 nm. Zhang *et al.*[25] studied the size effect on T_C and spontaneous polarization by using Laudau phenomenological theory. The theoretically predicted critical size is 4.2 nm which is smaller than the results from the empirical fitting mentioned above. Compared to $BaTiO_3$, one of the advantages of $PbTiO_3$ is that the phase transition is reversible and high-temperature cubic phase will spontaneously transform into tetragonal phase as temperature decreases below T_C, as observed in the epitaxial $PbTiO_3$ thin film obtained by metalorganic chemical vapor deposition.[26]

1.2 Ferro/ferrimagnetic Materials

In analogous to ferroelectric materials, a ferromagnetic material has spontaneous magnetization which can be tuned by applied magnetic field.[27] Ferromagnets contain spontaneously magnetized domains in which the net magnetic moment carried by parallel orientation of the individual atoms' magnetic moments. As shown in the magnetic hysteresis (Figure 1-3), the net magnetization of the unmagnetized ferromagnets could be zero due to different orientation of the magnetic domains.[28]

As the magnetic field (H) increases, reorientation of the domains makes the flux density B increase gradually from zero to the maximum value known as saturation induction B_s. When H is reduced to zero after saturation, the induction however only decreases from B_s to B_r, which is

called the residual induction. This is because the domain walls moved during the magnetization process do not return to the original position due to the defects in the crystal according to Barkhausen effect.[29] Extra reversed field is therefore required to reduce the induction to zero which is called the coercivity H_c. Another intrinsic property of ferromagnetic material is the saturation magnetization M_s. The saturation magnetization generally depends on the crystallographic direction due to spin-orbit coupling. The electron density associated with orbital angular momentum, cannot rotate freely with an arbitrary applied field direction. Therefore, along certain crystallographic directions, usually called easy axis, M_s can be achieved by applying low magnetic fields.[30]

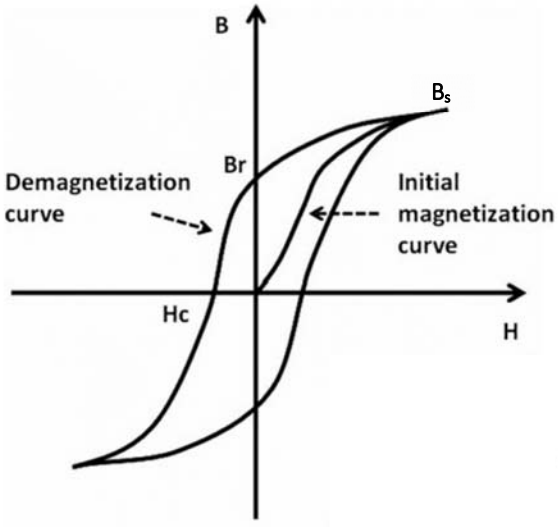

Figure 1-3: Hysteresis loop that includes the initial magnetization curve. Also shown are coercivity H_c and remanent magnetic flux density B_r. A hysteresis loop can be obtained by plotting magnetic field density B vs. applied magnetic field intensity H.[27]

Similar to ferroelectrics, above T_C, a ferromagnetic material undergoes a phase transition to a high-temperature paramagnetic phase that does not have spontaneous magnetization. From the view of quantum mechanics, for a ferromagnetic material, the unpaired electron spins from partially filled electronic shells align parallel to each other as a result of the exchange interaction.[31]

As the temperature increases, thermal agitation will compete with the exchange interaction and eventually become overwhelming when the temperature approaches T_C which will make random orientation of spins and turn the material to paramagnetic state.[32]

Ferrimagnetic materials are similar to ferromagnets in terms of the spontaneous and non-negligible magnetization. From the point of view of magnetic interaction between different ions in the crystal lattice, they are analogous to antiferromagnetic materials for which adjacent spins have opposite orientation. Usually, in ferrimagnets, the magnetic ions located at different lattice sites have antiparallel magnetic moment.[33] However, the resultant magnetization of the ions on one lattice site is stronger than the other site which gives a non-zero net magnetization. Ferrites are mostly found to be ferrimagnetic.[34]

Cobalt ferrite is one of the intensely investigated ferrimagnetic ferrites. As was shown in Figure 1-4, it has an inverse spinel structure in which O^{2-} anions are arranged in a cubic closed-packed lattice with metal cations surrounded octahedrally or tetrahedrally coordinated O^{2-} ions. Half of the Fe^{3+} ions occupy the tetrahedral sites (A sites) and the rest of the Fe^{3+} ions, along with all Co^{2+} ions, occupy the octahedral sites (B sites) in the crystal lattice. In the spinel structure ions sitting in A and B sites usually have oppositely oriented spins. As a consequence, the resultant magnetization of ions in one set of lattice sites is higher than that in the other, which results in ferrimagnetism. In general, $CoFe_2O_4$ is a ferrimagnetic oxide with Curie temperature of 793 K. The magnetic ordering of $CoFe_2O_4$ arises from several exchange couplings between different cations.[35] The predominant interactions are super-exchange interactions, in which Fe^{3+} and Co^{2+} couple through an overlap of their 3d orbitals with the 2p orbitals of an intermediate oxygen O^{2-}. Szotek *et al.*[36] calculated the electronic band structure for several ferrites, including $CoFe_2O_4$. A

theoretical band gap of 0.80 eV was calculated for $CoFe_2O_4$. They also calculated the exchange splitting of the conduction band, finding it to be 1.28 eV.

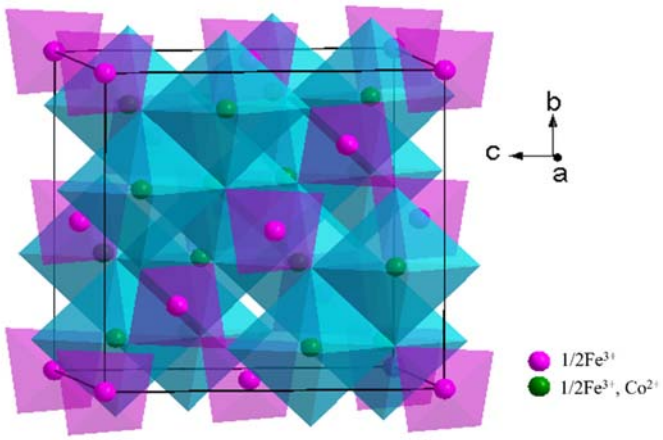

Figure 1-4: Schematic representation of the inverse spinel structure of $CoFe_2O_4$ with tetrahedral (A) and octahedral (B) sites. Pink spheres represent metal ions (half of Fe^{3+} ions) in A sites and green spheres represent metal ions (half of Fe^{3+} and all of Co^{2+} ions) in B sites. O atoms are located at the vertices of each polyhedron which are not shown in this figure.

$CoFe_2O_4$ NPs, like other ferromagnetic or ferrimagnetic NPs, also exhibit size-dependent magnetic properties. According to the Stoner-Wohlfarth theory[37], the magnetocrystalline anisotropy (E_A), which serves as an energy barrier to prevent the change of magnetization direction, is proportional to the particle size.[38] When the particle size decreases below a certain value, E_A will become comparable to the thermal activation energy k_BT (where k_B is Boltzmann constant). In this circumstance, the coercivity of the ferro/ferrimagnetic NPs will become negligible, as the direction of the magnetic moment can be easily changed. However, magnetic ordering still exists in NPs with relatively large magnetic moment. This behavior is known as superparamagnetism. Li *et al.*[39] compared their work on superparamagnetic $CoFe_2O_4$ NPs with other literature reports. They found that $CoFe_2O_4$ NPs become superparamagnetic when the particle size is smaller than 9 nm. Yu *et al.*[40] also found that the magnetic properties of spinel ferrite NPs are related to the atomic ratio of metal ions. In their work of cobalt doped ferrite ($Co_xFe_{3-x}O_4$) NPs, the coercivity increases

with increasing atomic percentage of cobalt until x in $Co_xFe_{3-x}O_4$ reaches 0.6. After that, continuing increase in the amount of cobalt results in a slight coercivity decrease, while the saturation magnetization increases.

1.3 Multiferroics

Multiferroics have been formally defined as materials that exhibit more than one primary ferroic order parameter.[41] Aside from the ferromagnetism and ferroelectricity mentioned above, there is another primary ferroic ordering called ferroelasticity. The strain of the ferroelastic material can be switched by applied stress. A Ferrotoroidics are materials whose ferroic ordering is switchable by crossed electric and magnetic fields. Generally, cross coupling of ferroic orderings can generate new properties such as ME effect, piezoelectricity, and piezomagnetism. For instance, in ME multiferroics, ME effect allows the magnetic properties to be tuned by external electric field.

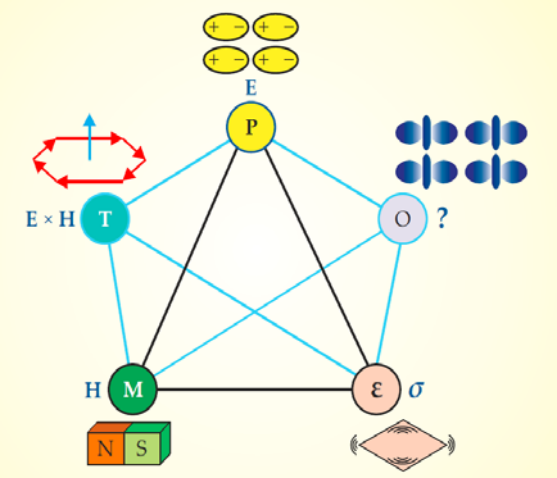

Figure 1-5: Interactions in multiferroics. Primary ferroic orderings, ferroelectricity (P), ferromagnetism (M), and ferroelasticity (ε), can be switched by their conjugate electric (E), magnetic (H), and stress (σ) fields, respectively[42]

Since the idea of multiferroics was first proposed, it has rapidly become the focus of research because of its promising future in many electromagnetic devices, such as magnetic field senor, electrically tunable microwave device, power conversion device, and computer

memory.[43,44,45,46] Zhai *et al.*[43] made bimorph and push-pull laminate composite magnetic field sensors which can achieve limit of detection down to pico-Tesla (10^{-12} T) at room temperature. Switching the magnetization of a magnetic material using external electric field in multiferroic films could make it possible to electrically tune the magnetization of magnetic microwave device such as, filters, oscillators, and phase shifters. In the work of Liu *et al.*,[44] giant electrostatically induced tunable magnetic resonance field at microwave frequencies was found in Fe_3O_4/PMN-PT (lead magnesium niobate-lead titanate) and Fe_3O_4/PZN-PT (lead zincniobate-lead titanate) multiferroic heterostructures. The ME effect in multiferroics, in analogy to piezoelectric effect which can be used to convert motion into electricity, can be utilized to generate electricity from the electromagnetic energy. Dong *et al.*[45] found strong voltage gain effect in multilayer structure consisting of magnetostrictive Terfenol-D ($Tb_{1-x}Dy_xFe_{2-y}$) and piezoelectric $Pb(Zr,Ti)O_3$. Traditionally, magnetization or ferroelectric polarization was used to store binary information in magnetic random access memories or ferroelectric random access memories, respectively. The multiferroic material which simultaneously has polarization and magnetization provide the chance to create four-state logic memories. Using this idea Gajek *et al.*[46] fabricated a $La_{2/3}Sr_{1/3}MnO_3/La_{0.1}Bi_{0.9}MnO_3$/Au (LSMO/LBMO/Au) tunnel junction, in which, four-resistance-state system was realized through tunnel electroresistance and its combination with tunnel magnetic resistance in LBMO-based spin filters.

1.3.1 Single-phase Multiferroics

In current convention, multiferroics mainly refers to materials which combine ferroelectricity and ferromagnetism or other types of long range magnetic ordering. Under this definition, the work regarding multiferroics can be tracked back to the research of MEs. In the 1970s, the group of Hans Schmid summarized the higher-order ME effect. This pushed forward

the development of multiferroics, which led to an expansion of research in the area.[47] In 1994, Schmid proposed the term 'multiferroic', which only refers to a single phase material which exhibits two or more primary orderings. However, the research activity in this new field quickly became static. In the last decade of the 20th century, many physicists were confused by the limited amount of single phase multiferroics in existence.

One of the main reasons behind the lack of single phase multiferroics is that most ferroelectric materials tend to be robust insulators. Even among insulating materials, if they have impurities or inexact ratios of atoms, the ferroelectric properties will be critically affected due to leakage current. When a magnetic element is present in ferroelectrics, associated secondary phases and defects can cause severe leakage problems.

Another reason for limited multiferroics is that at that time, proper ferroelectrics, in which spontaneous polarization was the first order parameter of lattice distortion, were well studied and expected to be the primary candidate for multiferroics. For these kinds of ferroelectric materials, polarization will arise if the non-magnetic cations shift away from the center of their surrounding anions. However, for magnetic materials, the magnetic cations tend to sit exactly on the center of their surrounding anions.[48] This is the well-known "d^0 vs d^n problem".

1.3.1.1 Introducing Ferroelectric Ordering into Magnetic Materials

In early 2000, several new mechanism of introducing ferroelectric ordering into magnetic materials were discovered in $BiFeO_3$[49], and $TbMnO_3$[50], which lit up this field again. In the perovskite-structure $BiFeO_3$, Fe^{3+}, with its five 3d electrons, provides magnetism, while the stereochemically active lone pair electrons of Bi^{3+} cause the necessary polar displacement of all the anion and cation sublattices relative to each other, which lead to the spontaneous electric polarization.[51] In the case of $TbMnO_3$, the spontaneous polarization is very similar to improper

ferroelectrics. Figure 1-6 shows the sinusoidal Mn^{3+} magnetic moment along the b direction when the temperature is below the Neel temperature ($T_N \approx 41$ K). Along <110> direction, Mn-O-Mn bonding forms a zigzag chain, as it undergoes the Jahn-Teller distortion. Kimura *et al.*[50] suggested that the Ising-type of Mn^{3+} magnetic moment can induce a displacement of O ions which in turn will cause spontaneous polarization. In addition to these two mechanisms, another way to induce ferroelectricity in multiferroics can be found in so called geometric multiferroics. In these materials, there is typically a layered compound that adopts unusual polar tilts and rotations of the anionic sublattice. A common example is barium nickel fluoride ($BaNiF_4$)[52], in which the ferroelectric distortions are driven by a combination of steric and electrostatic effects that are compatible with the presence of magnetic ions.

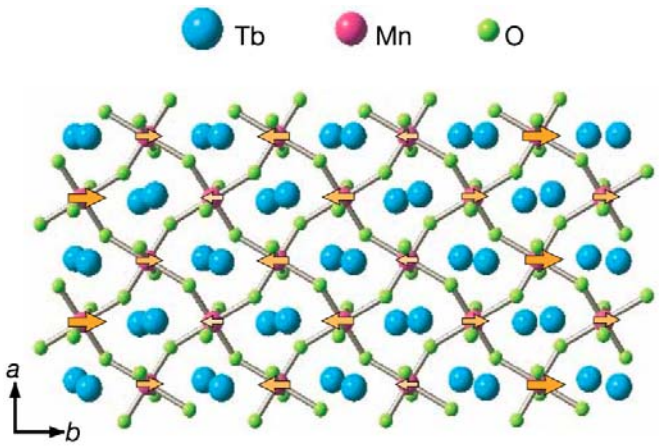

Figure 1-6: $TbMnO_3$ crystal structure under room temperature. The orange arrow denotes the magnetic moment of Mn^{3+} below T_N[50].

However, these single phase materials have some disadvantages, hampering their application. For example, Fe^{2+} and oxygen deficiency in $BiFeO_3$ can cause leakage current and degrade the electric polarization. In $TbMnO_3$, the achieved ferroelectricity is similar to the improper ferroelectrics, which makes the spontaneous polarization very small compared to the usual displacive ferroelectrics. Furthermore, the ME coupling amongst single phase multiferroics

is usually small except in $TbMnO_3$-type single phase multiferroics, in which the ferroelectricity is driven by magnetic structure, resulting in a strong coupling between them.

1.3.1.2 Introducing Magnetic Ordering into Ferroelectric Materials

As mentioned before, the magnetic ions with "d^n" electronic structure prefer the symmetric sites in crystal lattice which is not compatible with the conditions for having spontaneous polarization in ferroelectrics. Providing that the long range magnetic ordering has been realized in diluted magnetic semiconductor oxides (DMSOs) such as Ni-doped SnO_2[53], Co-doped ZnO[54], and Ni-ZnO[55], researchers attempted to dope the transition-metal ions into the ferroelectrics to introduce the magnetic ordering while keeping the ferroelectric properties. Son *et al.*[56] prepared the Mn-doped $BaTiO_3$ nanorods by applying the dip-pen nanolithography technique. The non-negligible magnetic hysteresis was observed under room temperature along with the piezoelectric hysteresis. Ling *et al.*[5] used Cr-doped $BaTiO_3$ nanocrystals (NCs) as the building block for the nanocrystalline thin films in which extended structural defects formed at NCs interfaces mediating long-range magnetic ordering of Cr^{3+} ions. Fe-doped $PbTiO_3$ NPs with the size range of 19-30 nm have been synthesized via sol-gel method and proved to be ferromagnetic and ferroelectric at room temperature.[57] However, the origin of ferromagnetism in ferroelectrics is still under debate, and recent theoretical studies consider oxygen vacancies mediated ferromagnetism as one possible explanation for the origin of ferromagnetism in these materials which, to some degree, is similar to the theory in the case of DMSOs.[58]

In DMSOs, the concentration of the magnetic cations usually is very low and well below the limit required for the conventional exchange interaction which traditionally is used to explain magnetic ordering in oxides. Coey *et al.*[59] discussed the ferromagnetic exchange coupling in DMSOs by using a new model of indirect exchange via shallow donors as shown in figure 1-7. In

this model, the shallow donor electrons originated from oxygen vacancies form magnetic polarons which can mediate the magnetic ordering. At low concentration of donors, their hydrogenic orbitals overlap to form the impurity band with localized electrons. As donor concentration increases above the critical concentration, the impurity band states would be delocalized. The donor impurity band will become spin-split due to the overlap of the magnetic polarons. Interaction between the electronic states of the localized 3d impurity band and delocalized donor states lead to an extended hybridized state which result in the high T_C.

Coey and the coauthors found that for the system containing mixed-valence magnetic ions, the magnetic ordering is not necessarily related to the exchange interaction of doped magnetic ions.[60] In the so-called charge-transfer ferromagnetism, the magnetic cations with mixed oxidation states facilitate the charge transfer between cations and local defects which will result in the rise of Fermi level to a peak of local density of states and the Stoner splitting of the defect band. This mechanism has been experimentally confirmed in the case of Mn-doped In_2O_3.[61]

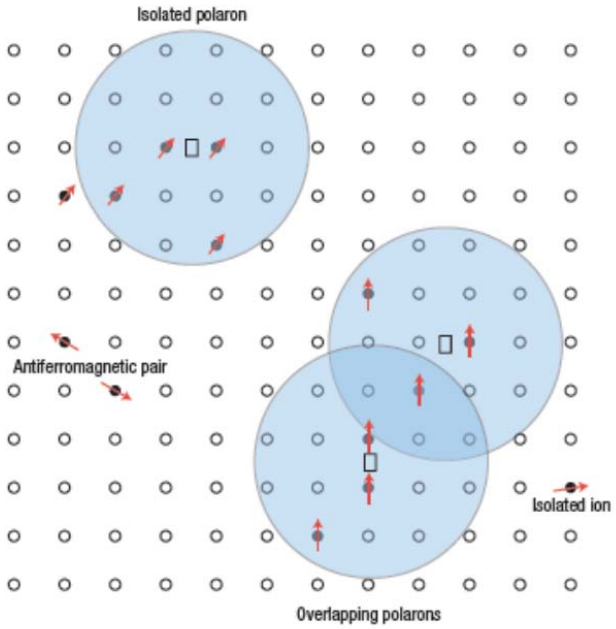

Figure 1-7: Representation of magnetic polarons. A donor electron in its hydrogenic orbit couples with its spin antiparallel to impurities with a 3d shell that is half-full or more than half-full. The figure is drawn for x (concentration of magnetic cations) = 0.1, $\gamma = 12$. Cation sites are represented by small circles. Oxygen is not shown; the unoccupied oxygen sites are represented by squares.[59]

1.3.2 Multiferroic Composites

The idea of multiferroic composites was initially proposed by Van Suchtelen *et al.*[62], who thought that composites of piezoelectric and magnetostrictive phases can be electromagnetically coupled via stress mediation. Since then, numerous combinations of different ferroelectric and ferromagnetic materials have been synthesized and investigated in order to obtain multiferroic composites. Among them, the $BaTiO_3/CoFe_2O_4$ heterostructure has been a focus of significant interest. Zheng *et al.*[63] fabricated nanostructured $BaTiO_3/CoFe_2O_4$ on single-crystal $SrTiO_3$ (001) substrates by pulsed laser deposition (PLD) method. This nanostructure, consisting of self-assembled hexagonal arrays of $CoFe_2O_4$ nanopillars embedded in a $BaTiO_3$ matrix, is shown in Figure 1-8. In this configuration, barium titanate functions as the ferroelectric part and cobalt ferrite as the ferrimagnetic part. The intrinsic similarities of the crystal structures of the perovskite

and spinel families lead to compatible lattice dimensions. For example, the lattice parameter of the perovskite structures is about 4 Å, which is within a 5% difference of the lattice parameter of the spinel structures. Zheng, H. *et al.*[63] found that ME coupling is dominated by the elastic interactions in two phase nanostructures.

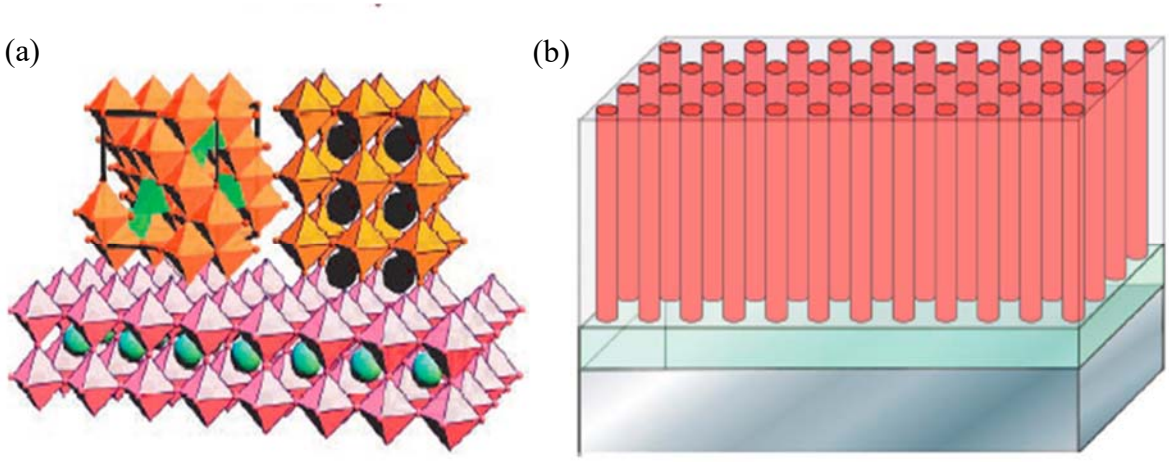

Figure 1-8: (a) Epitaxial alignment of a spinel (top left) and a perovskite (top right) on a perovskite substrate (bottom). (b) Schematic illustration of a self-assembled nanostructured thin film formed on the substrate.[63]

Inspired by the above result, several researchers have tried to use wet chemical methods to synthesize $BaTiO_3$-$CoFe_2O_4$ composites.[64,65,66,67] In these studies, a $BaTiO_3$-$CoFe_2O_4$ core-shell structure was synthesized by the sol-gel method in which the $CoFe_2O_4$ component was synthesized by coprecipitation and subsequently dispersed in the gel solution used to make $BaTiO_3$. However, in these cases, focus was placed on synthesis of the composite and the basic characterization of the ME properties. The mechanism of ME coupling for the $BaTiO_3$-$CoFe_2O_4$ multiferroic system was not discussed. As the research further develops, the fundamental mechanism for the ME coupling between two components of multiferroic composites become increasingly more important. Due to the merits of the PLD method, such as versatility, fast production, and scalability,

some ferroelectric/ferromagnetic multilayer structures were made via PLD in order to study the mechanism for ME coupling. Duan *et al.*[68] performed density functional theory calculations for $Fe/BaTiO_3$ (100) multilayers by constructing the supercell as $(Fe_2)_9$-TiO_2-$(BaO\text{-}TiO_2)_m$. Their calculations predicted that ferroelectric displacement of $BaTiO_3$ breaks the symmetry between the top and bottom interface, which can change the interface magnetization. The orbital-resolved local density of states of interface Ti and Fe ions suggested that the hybridization between Ti 3d and Fe 3d orbitals cause charge redistribution which induce the magnetic moment on Ti ions. In order to confirm the above prediction, a series of core @ shell-type $BaTiO_3$ @ Fe (or its oxides) were synthesized by sonochemical methods.[69] However, the Ti 2p X-ray magnetic circular dichroism (XMCD) signal for the synthesized core-shell structure is almost zero, which indicates that, for this system, the induced magnetic moment of interface Ti ions was negligible. Valencia *et al.*[70] later confirmed the prediction using a $Fe/BaTiO_3$ bilayer heterostructure grown by PLD. They determined the magnetic moment on Ti ions by recording the change of X-ray resonant magnetic scattering (XRMS) asymmetry of the Ti $L_{3,2}$-edge. Their results show the reverse of dichroism signal upon changing the helicity of light, which indicates the presence of magnetism on Ti ions. For the mechanism in ferrimagnetic/ferroelectric multiferroic composite systems, Schmitz-Antoniak *et al.*[71] performed X-ray absorption spectroscopy and its associated linear dichroism studies of the $CoFe_2O_4/BaTiO_3$ nanostructure. They found that due to the magnetostriction effect, under external magnetic field, $CoFe_2O_4$ nanopillars deform and produce shear stress on the hosting

$BaTiO_3$ matrix, which induces a transverse polarization component in $BaTiO_3$. However, the interfacial effect mentioned above in $Fe/BaTiO_3$ was not well explored in this system.

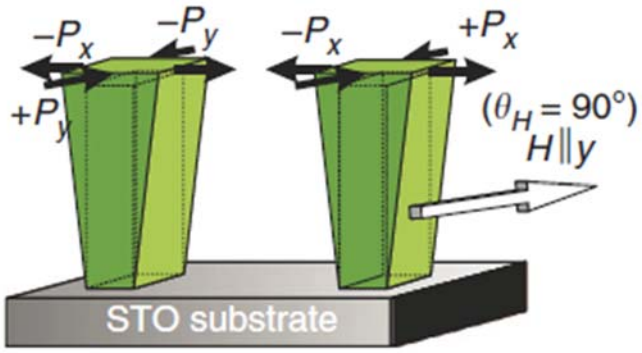

Figure 1-9: Illustration of experimental geometry and (deformed) shapes of CFO nanopillar's unit cells within apical polarization vector of the BTO environment ±Px,y.[71]

1.4 Motivations and Scope of the Thesis

The primary goal for this project is to synthesize multiferroic materials by different methods and different components. As mentioned before, Cr-doped $BaTiO_3$ nanocrystalline film has been demonstrated to exhibit long range magnetic ordering. Mn-doped $BaTiO_3$ could be another interesting material to be explored due to the possibility of mixed oxidation states of Mn ions in oxides which might introduce ferromagnetism through a different mechanism. In addition, composites consist of ferroelectric $BaTiO_3/PbTiO_3$ and ferrimagnetic $Co_{0.6}Fe_{2.4}O_4$ will be prepared with different method followed by systematic investigation to find the rational design for the multiferroic structure.

This study began with synthesis of Mn-doped $BaTiO_3$ and study of its electric and magnetic properties. Then pure $BaTiO_3$ NPs with different size and $Co_{0.6}Fe_{2.4}O_4$ NCs were synthesized to obtain the building blocks with optimized electric and magnetic properties. Different methods, including impregnation and a spin coating method, were utilized to combine the two components together and form the effective interface. As a next step, various characterization methods will be

applied for both components and the composite in order to obtain the structural information and the corresponding magnetic or electric properties. Finally, nanostructured $PbTiO_3$ with robust ferroelectric properties was prepared to incorporate with ferrimagnetic component to produce more practical multiferroic composites.

Chapter 2 Experimental Section

2.1 Materials

Iron(III) chloride hexahydrate ($FeCl_3 \cdot 6H_2O$, 97%) was purchased from BDH Chemicals. Sodium oleate ($C_{18}H_{33}NaO_2$, 97%) was obtained from TCI America. Manganese(II) acetylacetonate, ($Mn(acac)_2$, 97%) was purchased from Avocado Research Chemicals. Sodium hydroxide (NaOH, 97%) was obtained from Caledon Laboratories. Barium rods (Ba, 99%), barium chloride anhydrous ($BaCl_2$, 98%), cobalt(II) chloride hexahydrate ($CoCl_2 \cdot 6H_2O$, 98%), iron(III) acetylacetonate ($Fe(acac)_3$, 99%), and titanium(IV) isopropoxide ($Ti(O\text{-}i\text{-}Pr)_4$, 98%), were purchased from Strem Chemicals. Trioctylphosphine oxide (TOPO, 90%), benzyl alcohol ($C_6H_5CH_2OH$, 99%), 1-Butanol ($CH_3(CH_2)_3OH$, 99.7%), benzyl ether ($(C_6H_5CH_2)_2O$, 98%), titanium(IV) butxoide ($Ti(O\text{-}Bu)_4$, 97%), toluene, hexane and ethanol were obtained from Sigma Aldrich. Oleic acid ($CH_3(CH_2)_7CH{=}CH(CH_2)_7COOH$, 90%), and cobalt(II) 2,4 pentanedionate ($Co(acac)_2$), and lead(II) oxide (PbO, 99.999%) were purchased from Alfa Aesar. All the reagents were used as supplied by the manufacturer without further purification. For the solvothermal treatment, Parr acid-digestion bombs with 45 mL Teflon liners were used.

2.2 Synthesis and Sample Preparation

2.2.1 Synthesis of $BaTiO_3$ NPs

The procedure for synthesis of $BaTiO_3$ NPs has been developed by Ju *et al*..[5] First, 3 mmol metallic Ba pieces were dissolved in benzyl alcohol by heating the solution to 353 K under vacuum. Then, the solution was cooled down to room temperature and 3 mmol $Ti(O\text{-}i\text{-}Pr)_4$ was added to the solution as the titanium source. After that, the solution was stirred overnight followed by centrifugation to obtain a gel-like precipitate. The precipitate was thoroughly mixed with water and transferred to the acid digestion bomb for the hydrothermal synthesis at 473 K for 48 h. The

product was isolated by centrifugation and washed with ethanol three times. The clean NPs were dispersed in melted TOPO at 423 K for 1 h and precipitated with ethanol. Centrifugation and washing with ethanol were performed to eliminate uncapped TOPO on the NP surfaces. The above TOPO treatment and ethanol washing process was repeated three times. The TOPO-treated NPs were then suspended in oleic acid at 393 K and stirred for 30 min. The final products were dried and crushed with a mortar and pestle and stored for further studies.

2.2.2 Synthesis of Mn-doped $BaTiO_3$ NPs

Mn-doped $BaTiO_3$ NPs were synthesized using the same method mentioned above. $Mn(acac)_2$, as Mn dopant precursor, was added into benzyl alcohol with metallic Ba in this experiment. In addition, in order to obtain NPs with different sizes, water, ethanol, and benzyl alcohol were used as solvents to mix with the gel-like precipitate before the mixture was transferred into 45 mL acid digestion bomb. After the NPs were obtained, TOPO treatment followed by ethanol washing was applied and repeated twice to completely remove the surface-bound dopant ions. Finally, TOPO-treated NPs were dispersed in hexane for further characterization.

2.2.3 Synthesis of $BaTiO_3$ NPs with Small Size

The method used for synthesis of small $BaTiO_3$ NPs was developed by Adireddy *et al.*.[19] Four solutions including 5 mL $BaCl_2$ (1 mmol) aqueous solution, 5 mL NaOH (12.5 mmol) aqueous solution, a mixture of 2.5 mL oleic acid and 5 mL butanol, and a mixture of 1mmol $Ti(O\text{-}Bu)_4$ and 5 mL butanol were prepared separately and then transferred to an 45 mL acid digestion bomb. The bomb was then put into the oven and heated to 408 K for 18 h. After that, the NPs were

collected by centrifugation and washed with ethanol three times. Finally, $BaTiO_3$ NPs were dispersed in toluene.

2.2.4 Synthesis of $CoFe_2O_4$ NPs

The cobalt ferrite NPs were synthesized using methods based on the liquid-solution-solid process.[39] 3 mmol of $FeCl_3 \cdot 6H_2O$ and 1.5 mmol $CoCl_2 \cdot 6H_2O$ were dissolved in 20 mL water and 10 mL ethanol. 12 mmol sodium oleate is then added to the solution with 2 mL oleic acid and the solution was stirred vigorously for 2 h. The solution was then placed in two 45 mL Teflon lined acid digestion bombs (Parr) and put into a 453 K oven for 12 h. Once the reaction was complete, the digestion bombs were removed and left to cool in the air. After the digestion bombs had cooled to room temperature, hexane was added to the solutions and a liquid-liquid separation was performed to remove the aqueous phase. $CoFe_2O_4$ NPs were washed three times with ethanol. Following washing, the obtained NPs were suspended in hexane.

2.2.5 Synthesis of $Co_{0.6}Fe_{2.4}O_4$ NCs

The synthesis of $Co_{0.6}Fe_{2.4}O_4$ NCs was based on the method proposed by Yu *et al.*.[40] 1 mmol $Fe(acac)_3$, 0.48 mmol $Co(acac)_2$, 1 mmol sodium oleate, and 2 mL oleic acid were mixed with 10 mL benzyl ether and stirred under argon atmosphere. The mixture was heated to 393 K and kept at this temperature for 1 h, followed by increasing the temperature to 563 K for another 1 h. After that, the solution was cooled down to room temperature naturally. The NCs were isolated by adding a mixture of hexane and ethanol with a 1:3 volumetric ratio and subsequent centrifugation for 10 min. The synthesized NCs were washed with ethanol three times and finally dispersed in toluene.

2.2.6 Synthesis of $BaTiO_3/Co_{0.6}Fe_{2.4}O_4$ Composite by Impregnation Method

The synthesized $BaTiO_3$ NPs were dispersed in the $Co_{0.6}Fe_{2.4}O_4$ NCs toluene suspension and then sonicated for 1h. After that, the mixed solution was left overnight to allow the product to settle out of the solution. The toluene suspension containing $Co_{0.6}Fe_{2.4}O_4$ NCs was removed and the product was washed with ethanol three times. The final products were dried, annealed at 373 K for 3 h, and then crushed with a mortar and pestle and stored for further studies.

2.2.7 Synthesis of $BaTiO_3/Co_{0.6}Fe_{2.4}O_4$ Multilayer Films by Spin-coating Method

The multilayer structure was prepared by alternating spin coating of a toluene suspension of small $BaTiO_3$ NPs (obtained from the synthesis in Chapter 2.2.3) and the $Co_{0.6}Fe_{2.4}O_4$ NCs on clean sapphire substrates. The films on sapphire substrates were annealed at 373 K for 10 min between consecutive coatings. The entire process was done under a magnetic contamination-free environment. The above procedure was repeated several times until the mass of the sample is above 1.0 mg.

2.2.8 Synthesis of $PbTiO_3/Co_{0.6}Fe_{2.4}O_4$ Multilayer Films by Spin-coating Method

In order to get the crystalline $PbTiO_3$ thin film, amorphous sample was synthesized as building block via hydrothermal synthesis. PbO-oleic acid complex was prepared by dissolving 1 mmol PbO into 2 mL oleic acid at 373 K and added into 20 mL benzyl alcohol with 1 mmol $Ti(O\text{-}Bu)_4$ and 2 mL oleic acid under stirring. Then the solution was mixed with 1mL H_2O and transferred into a 45 mL acid digestion bomb for hydrothermal reaction at 473 K for 48 h. The sample was precipitated and washed with ethanol followed by dispersing into toluene to obtain the transparent suspension for spin-coating. $PbTiO_3$ and $Co_{0.6}Fe_{2.4}O_4$ suspension were alternately spin-coated on the quartz film with annealing at 773 K for 3 h to obtain the multilayer structure.

2.2.9 Synthesis of $PbTiO_3$ Nanoribbons

$PbTiO_3$ nanoribbons were synthesized by modifying the method proposed by Hu *et al.*.[72] In a typical synthetic process, 1 mmol $Ti(O\text{-}Bu)_4$ was mixed with 2 mL ethanol and added dropwise into 10 mL aqueous solution containing 1 mmol $Pb(CH_3COO)_2 \cdot 3H_2O$. A various amount of NaOH was added into the mixed solution as mineralizer. The mixed solution was stirred for 30 min and then transferred into a 45 mL acid digestion bomb. The autoclave was kept in a 473 K oven for 18 h. After the reaction was complete, the acid digestion bomb was cool down to room temperature naturally, and the products were precipitated and washed with ethanol for three times. The final products were dried and crushed with a mortar and pestle and stored for further studies.

2.3 Characterization Techniques

2.3.1 Powder X-ray Diffraction

Powder X-ray diffraction (XRD) is a common characterization method for crystal structure of materials. In addition to the lattice parameter, the crystallite size can also be estimated through the Debye-Scherrer equation:

$$T = \frac{C\lambda}{B\cos\theta}$$

where T is the crystallite thickness, C is the dimensionless shape factor with the value close to 1, λ is the wavelength of the X-rays (1.54 Å), θ is the diffraction angle in radians, and B is the full-width at half-maximum (FWHM).

The measurements were performed with an INEL XRD diffractometer in Dr. Holger Kleinke's group in Department of Chemistry at the University of Waterloo. The diffractometer is equipped with a position-sensitive detector, utilizing monochromatic Cu-Kα radiation (λ = 1.5406 Å).

2.3.2 UV-Visible (UV-vis) Absorption Spectroscopy

UV-vis absorption spectroscopy refers to absorption spectroscopy in the ultraviolet-visible light region. Generally, it is used to detect electronic transitions from the ground state to excited states. The electronic transition of the transition-metal involved in this project can be studied using this method. Without the ligand field, the five degenerate d orbitals of transition-metal ions will have the same energy. However, when the transition-metal is coordinated with ligands, the d orbitals will split in energy. Considering an octahedral ligand field, the five degenerate d orbitals

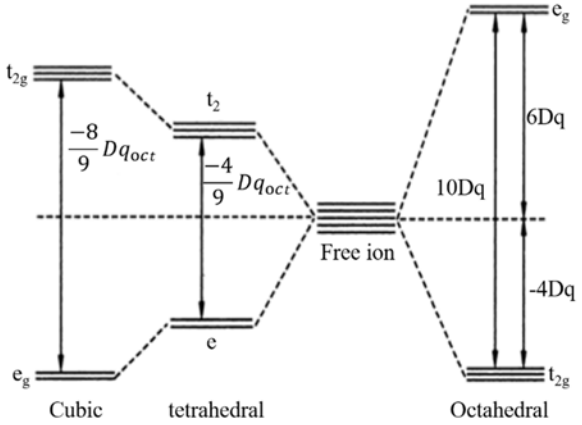

Figure 2-1: The d orbital splitting in cubic, tetrahedral and octahedral crystal field[73]

will split to $d_{x^2-y^2}$ and d_{z^2} orbitals with a higher energy (e_g), and d_{xy}, d_{yz} and d_{xz} orbitals with a lower energy (t_{2g}),[73] as shown in Figure 2-1.

The UV-vis absorption spectra were collected with a Varian Cary 5000 violet-visible-near infrared (UV-vis-NIR) spectrophotometer using 1 cm path-length quartz cuvettes.

2.3.3 Raman Spectroscopy

Normally, Raman spectroscopy can be used to collect the vibrational information of the material by the shift of the frequency of scattered laser photons. Furthermore, the vibrational information can be correlated to the strength, length and the arrangement of the chemical bond.[74] In the case of solid-state material, the characteristic phonon modes can be detected by Raman

spectroscopy and used to identify the substance. In addition, even for the same material, the phonon mode could be different for different crystalline phases with different symmetry element which makes Raman spectroscopy a really sensitive technique to confirm the crystal structure of a certain material.[75,76] In this project, Raman spectroscopy is mainly used to confirm the tetragonality of the synthesized $BaTiO_3$ and $PbTiO_3$ samples which is crucial for the ferroelectric properties. It is also used to study the effect of size and temperature on the phase transformation of the ferroelectric materials.

Raman spectroscopy was performed at room temperature with a Renishaw 1000 spectrometer using He-Ne laser with the excitation wavelength of 632.8 nm in Giga-to-Nanoelectronics Center at the University of Waterloo. The radiation source employed was 10% of the total output power (40mW). Prior to the measurement, the spectrometer was calibrated using a silicon foil.

2.3.4 Electron Microscopy

The morphology and particle sizes were confirmed by both scanning electron microscopy (SEM) using a LEO FESEM 1530 microscope operating at 7 kV in Waterloo Advanced Technology Lab at the University of Waterloo, and transmission electron microscopy (TEM) using a JEOL-2010F microscope operating at 200 kV at the Brockhouse Institute for Materials Research. Gatan Digital Micrograph software was used to measure the d-spacing from HRTEM images.

2.3.5 Magnetization Measurement

The magnetization was measured with the physical property measurement system (PPMS, Quantum Design) in ACMS mode, with a helium cooling system, allowing a wide range of temperatures from 2 to 400 K and magnetic fields up to ± 9 Tesla. The overall effective magnetic moment can be measured as a function of temperature or the applied magnetic field sweeping from a positive to a negative one, monitoring magnetic properties. Samples for PPMS measurement were prepared under magnetic contamination-free environment. Normally, NCs suspensions were spin coated on a clean sapphire substrate with annealing at 573 K for 1 min between two consecutive coatings (Figure 2-2). While for the $BaTiO_3/CoFe_2O_4$ multilayer sample, the annealing temperature was controlled at 373 K considering the phase transformation of $BaTiO_3$ happens at 393 K.

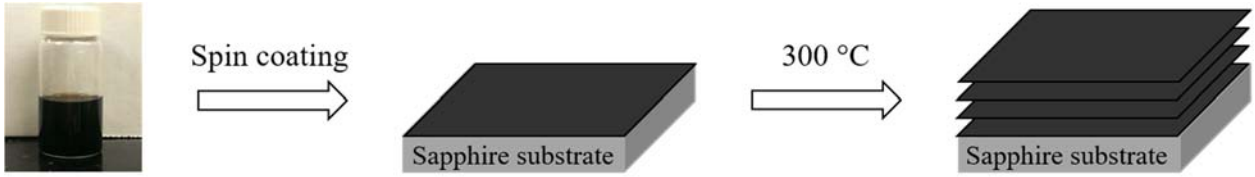

Figure 2-2: scheme of sample preparation of films from colloidal $Co_{0.6}Fe_{2.4}O_6$ for magnetization measurements.

2.3.6 X-ray Absorption Spectroscopy

X-ray absorption spectroscopy (XAS) is a unique tool to probe the local structure around element of interest within a material at the atomic or molecular scale. It covers a wide range of materials from crystalline to amorphous materials. XAS measures the absorption coefficient (μ(E)) as a function of X-ray energy E.[77] Normally, there is a sharp increase of μ(E) at the particular energy, called absorption edge, which corresponds to electrons reach the first available energy levels by absorbing the energy from incident photons. Then based on the relative position to the absorption edge, the X-ray absorption spectrum is divided into three main regions, namely X-ray

absorption near edge structure (XANES) which is a few eVs around the absorption edge containing fine structures, pre-edge and extended X-ray absorption fine structure (EXAFS) which locate before and after the near edge region, respectively. The analysis of XANES provides the information about the electronic structure such as oxidation states and spin states.

X-ray magnetic circular dichroism (XMCD) is recognized as a powerful method to probe the origin of long range magnetic ordering in magnetic materials. XMCD is obtained from the difference of two X-ray absorption spectra measured with left and right circular polarized light. In transition metals, the magnetic interactions originate from the partially filled d-orbitals.[78] X-ray absorption spectroscopy will thus be a powerful technique to further understand the electronic and magnetic properties of the magnetic materials. Since X-ray absorption techniques obey the dipole selection rules, the valence d states can be directly probed by excited 2p core electrons (L-edge spectroscopy). The L-edge studies spectra consist of two main features, $2p_{3/2}$ (LIII) and $2p_{1/2}$ (LII), which arise from the spin-orbit interaction between 2p core electrons. The ferromagnetic nature of transition metals can be studied using XMCD technique. In XMCD, left and right circularly polarized X-rays can excite a 2p-electron to partially filled 3d orbitals and transfer the angular momentum to the excited photoelectron at the same time. The spin-split valence shell will act as a spin detector for the excited photoelectron. The spin moment can be correlated quantitatively to a measured spectrum by a powerful XMCD sum rule.[79]

XAS can be obtained through several different conditions or modes including transmission mode, fluorescence mode and total electron yield method. In transmission mode, the absorption coefficient in this method follows the Beer-Lambert law: $\mu(E)x = \ln (I_0/I)$. In this mode where the intensity of the beam is measured before (I_0) and after (I) passed through the sample. It is one of the most widely used modes of detecting the absorption from the sample. The total electron yield

method works based on the fact that the total flux of photoelectrons is a function that is proportional to the absorption coefficient of a given element. This type of detection allows the user to overcome the thickness problem since the photon is not required to cross the sample to be detected. So in terms of the study of thin or thick films on a dense substrate, total electron yield mode is the best even with the compromise of a lower signal to noise ratio compared the transmission mode. The fluorescence mode is good for the study of very dilute element in transparent host materials due to low absorption edge.

In this project, XAS measurements of Mn-doped $BaTiO_3$ samples were performed at the SGM beamline (11ID-1) under total electron yield mode in Canadian Light Source, Saskatchewan. The sample was taken as a powder on the carbon tape on the Cu sample holder and then mounted into the SGM sample chamber. For Mn L-edge the energy was scanned in the range of 633 to 660 eV. XMCD measurements for the $CoFe_2O_4/BaTiO_3$ composite was performed in scanning transmission X-ray microscopy (STXM) configuration at the SM beamline (10ID-1) of the Canadian Light Source (CLS). The sample was dispersed in methanol and then deposited on the sample holder window. The sample holder was mounted on a magnetic ring (ca. 0.1 T), allowing for a parallel orientation of the magnetic field and X-ray beam propagation directions. The image stacks were collected at ca. 300 K by imaging a selected area of the sample with different energies at the Co $L_{2,3}$ edge from 770 to 810 eV, Fe $L_{2,3}$ edge from 700 to 735 eV, and Ti $L_{2,3}$ edge from 452 to 477 eV, using both left-circularly polarized (LCP, ρ^-) and right-circularly polarized (RCP, ρ^+) photons. The analysis of the images and spectra was performed using Axis 2000 software after the images were aligned using Jacobson Analysis software.

Chapter 3 Study of Mn-doped $BaTiO_3$ Nanoparticles

3.1 Structures Determined by X-ray Diffraction

Figure 3-1 shows representative XRD patterns of Mn-doped $BaTiO_3$ NPs synthesized in water, ethanol, and benzyl alcohol with the same starting Mn/Ti precursor molar ratio of 10%. The XRD patterns of all samples are in good agreement with the reference patterns of cubic or tetragonal $BaTiO_3$. The average grain size, obtained from Scherrer equation, for ethanol- and benzyl alcohol- synthesized Mn-doped NPs is estimated to be 6.2 nm and 4.0 nm, respectively. Around 45 degrees, the single (200) peak of cubic $BaTiO_3$ structure splits into two peaks of (200) and (002) of the tetragonal phase, which is usually used to distinguish cubic and tetragonal $BaTiO_3$.[80] In this study, the line width broadening caused by the short coherence length of the small NPs makes it challenging to exactly determine the crystal structure.

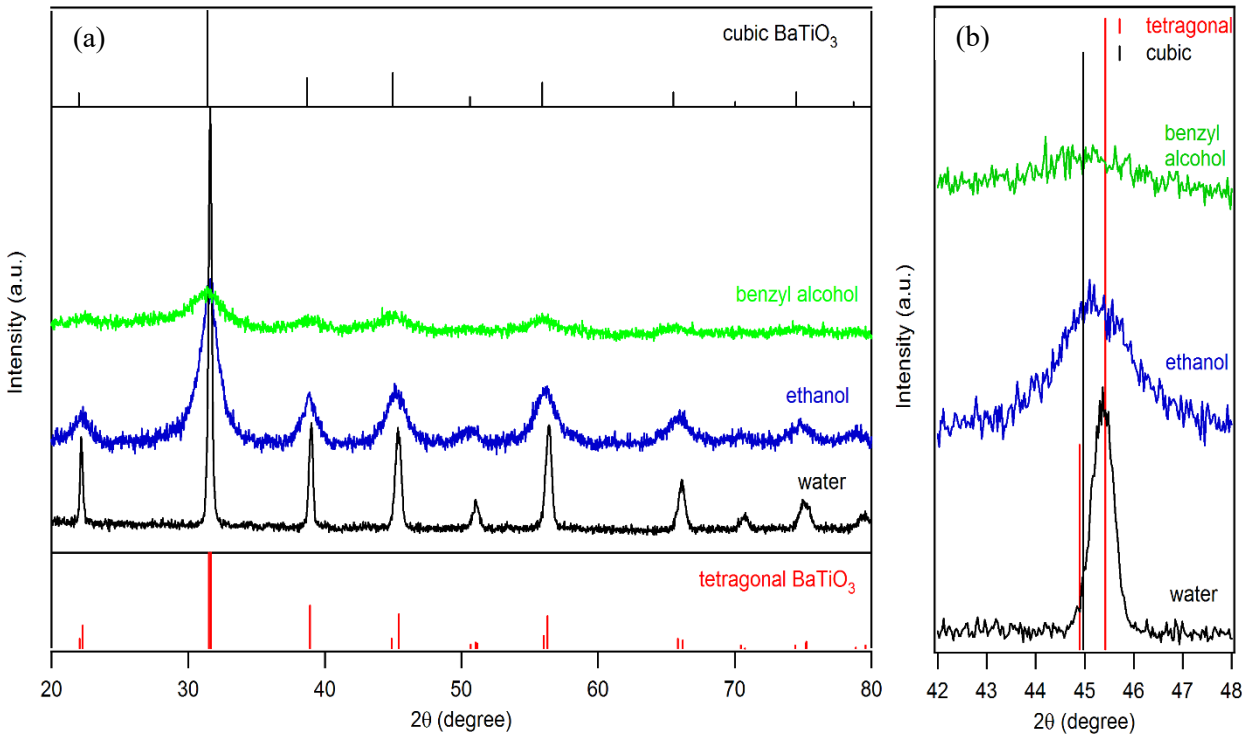

Figure 3-1: (a) Representative XRD patterns of Mn-doped $BaTiO_3$ samples synthesized in water, ethanol, and benzyl alcohol. The vertical black and red lines correspond to the XRD patterns of bulk cubic (JCPDS

no. 31-0174) and tetragonal (JCPDS no. 05-0626) $BaTiO_3$, respectively. (b) Enlarged XRD pattern around cubic (200) peak and tetragonal (200) and (002) peaks.

A difference can still be observed in the enlarged XRD patterns between the region around cubic phase (200) reflection peak and tetragonal phase (200) and (002) peaks. The peak for water-synthesized sample is located at the same position of tetragonal (200) reflection peak which corresponds to a large degree of tetragonal distortion of the sample. On the other hand, for the sample prepared in ethanol, the center of the gravity of the peak shifts to a lower 2θ value indicating the phase transformation from tetragonal to cubic phase. In addition, the slightly asymmetric shape of the peak and the appearance of a should coinciding with the peak maximum observed for the water-synthesized sample, might be attributed to the coexistence of both cubic and tetragonal phase. Peak positions of the benzyl-alcohol synthesized sample cannot be accurately determined from the XRD pattern due to the weak intensity and large boradening.

3.2 Morphology

TEM images of representative Mn-doped NPs synthesized in water, ethanol, and benzyl alcohol are shown in Figure 3-2. The NPs synthesized in water have a quasi-spherical geometry with particle size in the range of 100-200 nm. The nanocrystals prepared in ethanol and benzyl alcohol have sheet or platelet-like structure with average sizes of 6.4 ± 1.1nm and 4.6 ± 0.8 nm, respectively. Particle size determined from TEM images is consistent with the calculated value based on the Debye-Scherrer analysis of the XRD patterns. The insets in Figure 3-2 shows that all samples are single-crystalline. The lattice spacing of water-, ethanol-, and benzyl alcohol-synthesized Mn-doped NPs is measured to be 2.82 Å, 2.84 Å, and 2.86 Å, respectively. The lattice spacing of $BaTiO_3$ (110) plane is 2.825 Å for tetragonal phase and 2.85 Å for cubic phase. Although the measured lattice spacing indicates NPs prepared in water is mostly tetragonal, NPs

synthesized in benzyl alcohol are mostly cubic. It is difficult to unambiguously assign the lattice spacing to these two phases due to uncertainty of the measurements.

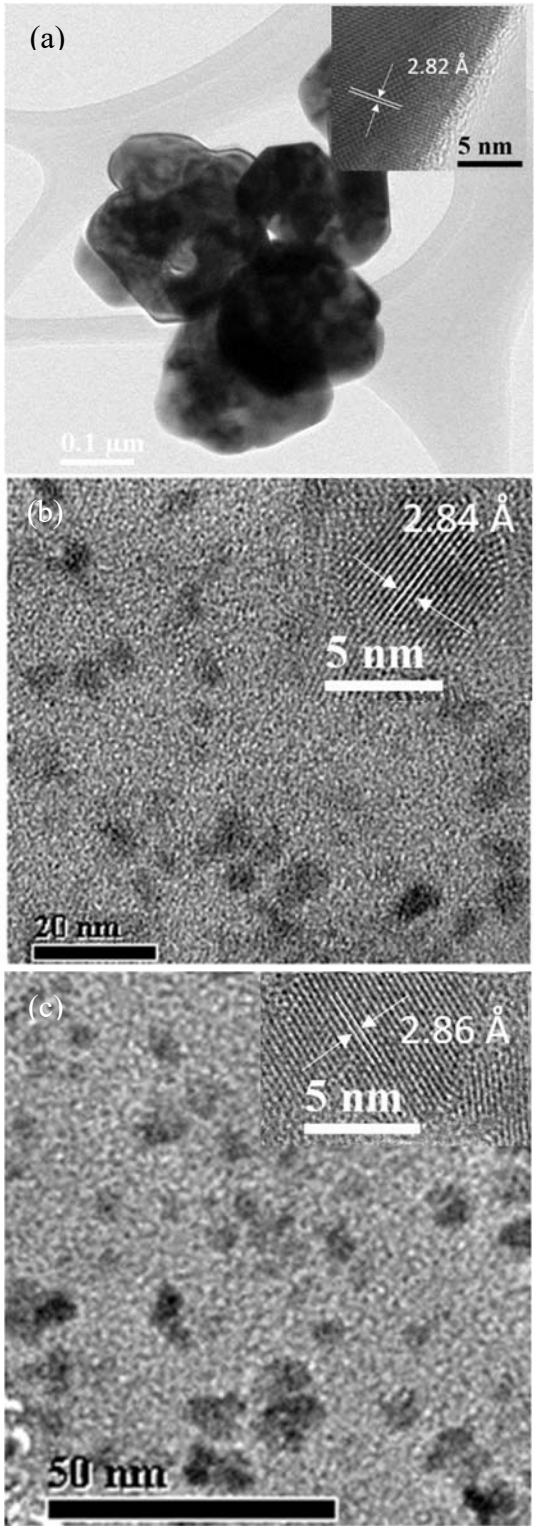

Figure 3-2: Representative TEM images of Mn-doped $BaTiO_3$ synthesized in (a) water, (b) ethanol, and (c) benzyl alcohol. The insets: High resolution TEM images showing measured lattice spacing.

The influence of different solvents on the growth of NPs is associated with their dielectric constant, the corresponding solubility of the precursor, and the steric hindrance of the solvents.[5,81] In addition to the observation of our TEM images of NPs prepared in water, it is likely that water also induces the aggregation of NPs with smaller size which leads to the formation of much larger NPs. As a result, the hollow structure might be formed during the hydrothermal process which has been observed in the template-free hydrothermal synthesis of different metal oxides materials such as TiO_2[82], ZnO[83], and Fe_2O_3[84]. The scanning TEM-energy dispersive X-ray spectroscopy (STEM-EDX) line scan profile of all elements is shown in Figure 3-3. The profiles of Ba (green line), Ti (purple line), and O (red line) have the same form displaying two peaks separately by a dip, indicating the same stoichiometry throughout the entire range. In addition, the line profiles for Ba and Ti elements are almost identical confirmiung the 1:1 molar ratio between Ba and Ti in the synthesized sample. The quantitative molar ratio

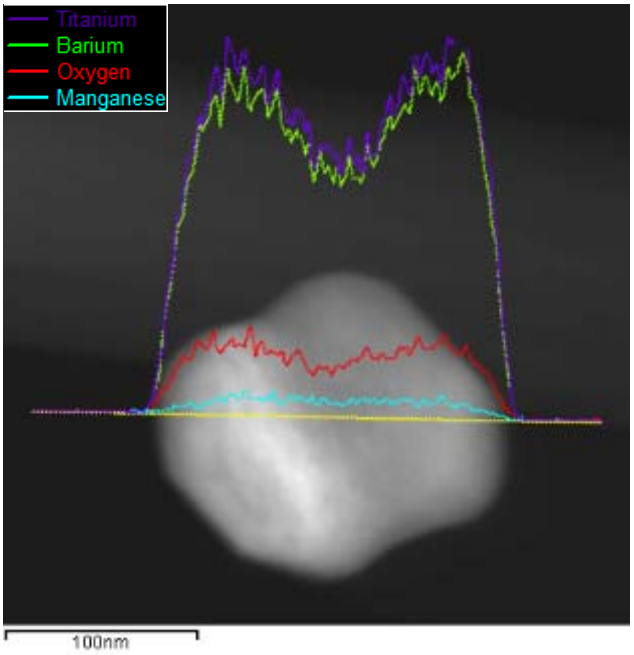

Figure 3-3: STEM image of a single Mn-doped $BaTiO_3$ nanoparticle with the EDX line scan profile on top of it. The inset shows the corresponding element of lines in line scan profile.

of Ba to O cannot be estimated based on the line scan profile due to the detection limit of EDX for oxygen.[85,86] Importantly, the line profile for Mn coincides with the line profiles for the elements of the host lattice, indicating homogeneous distribution of dopant ions and confirming the absence of secondary phases. Furthermore, the line scan counts decrease as the electron beam moves from the edge of the nanoparticle to its center suggesting the presence of a void which indicates the hollow structure of the water-synthesized NPs.

3.3 Phase Transition Determined by Raman Spectroscopy

Compared to the average and static crystal symmetry given by XRD, Raman spectroscopy can be used to study the local and dynamic symmetry which makes it an alternative effective method to identify the crystal phase of $BaTiO_3$. Normally, tetragonal $BaTiO_3$ has 10 Raman-active modes. $BaTiO_3$ with ideal cubic symmetry should be completely Raman-inactive. However, broad peaks centered at 260 cm^{-1} and 520 cm^{-1} have been observed in the cubic phase, which were attributed to the disorder of titanium sites.[87] Figure 3-4 shows the Raman spectra of as-synthesized NPs and the commercial bulk $BaTiO_3$. The peaks present in the Raman spectrum of commercial bulk $BaTiO_3$ powder are in agreement with that for the tetragonal phase, as expected. The disappearance of the E(LO+TO), B_1 peak at ~ 300 cm^{-1} and the A1(LO), E(LO) peak at ~ 715 cm^{-1} was used as an indication of the tetragonal-to-cubic phase transition.[75] The spectrum of Mn-doped sample prepared in water clearly shows the peaks centering at 300 cm^{-1} and 716 cm^{-1}, meaning that these NPs are in the tetragonal phase. Compared to the spectrum of bulk $BaTiO_3$, weakening and broadening of the characteristic peaks indicates relatively lower tetragonal distortion in water-synthesized sample. The intensities of these two peaks dramatically decrease

in the spectra of the sample prepared in ethanol and benzyl alcohol. However, there is still a noticeable difference in the spectra of ethanol and water-synthesized samples in the range of 200 to 360 cm^{-1}. The spectrum of ethanol-synthesized sample still shows a broad peak at ~ 300 cm^{-1} with relatively low intensity. Along with the weak and broad peak around 716 cm^{-1}, the NPs prepared in ethanol is likely to have some degree of local tetragonal structure which might undergo long-range ordering throughout the entire lattice. These two peaks completely vanish in the spectra of benzyl alcohol-synthesized sample which suggests the sample is mostly in cubic phase.

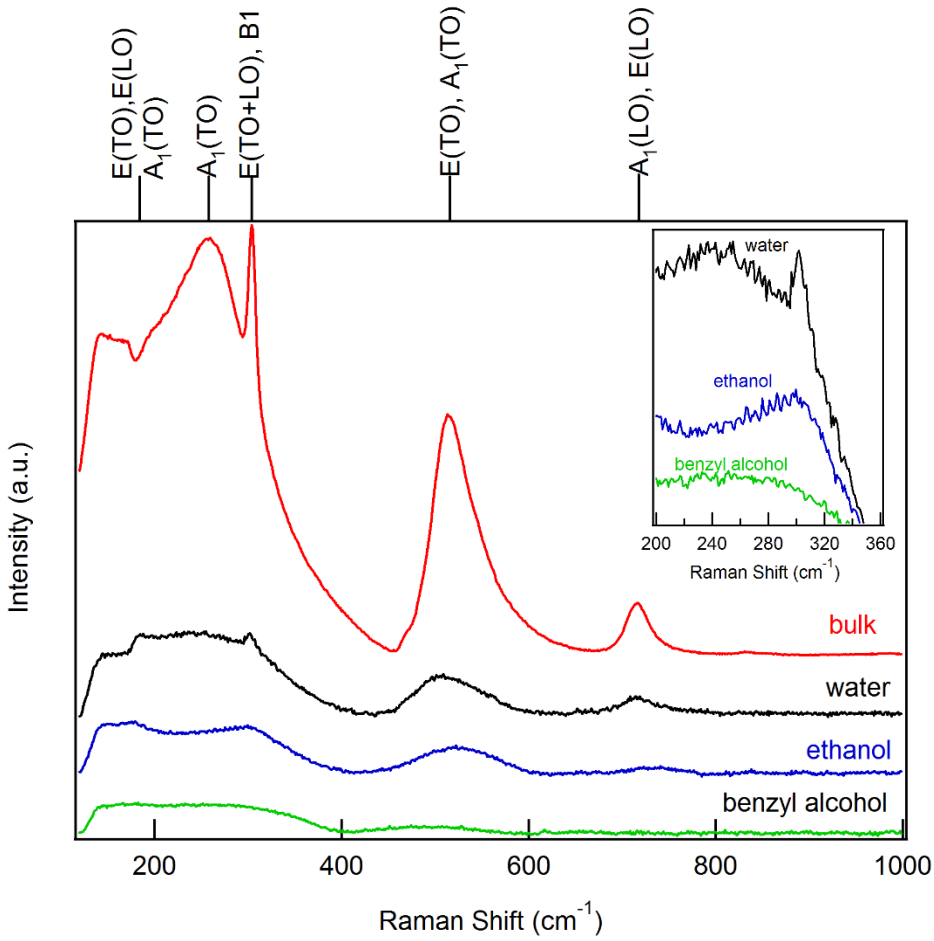

Figure 3-4: Raman spectra of Mn-doped $BaTiO_3$ NPs synthesized in different solvents and commercial powder (red trace) as comparison. The assignments of the Raman modes are indicated at the top of the figure. Inset: enlarged spectra of in the E(TO+LO), B_1 region (ca. 300 cm^{-1}) for NPs prepared in water (black), ethanol (blue), and benzyl alcohol (green).

3.4 Effect of Dopant Ions in Ethanol-Synthesized Mn-doped $BaTiO_3$

In order to get dispersed Mn-doped $BaTiO_3$ NPs with relatively high doping concentration which retain ferroelectric properties, NPs prepared in ethanol with different starting Mn/Ti molar ratio were investigated in a similar way as mentioned above with XRD and Raman spectroscopy. Figure 3-5 shows the XRD patterns of the NPs synthesized in ethanol with different starting Mn/Ti ratios of 5%, 10%, and 15%. There is no obvious broadening of peaks observed among all three patterns which suggests similar size of samples synthesized with different Mn/Ti molar ratio. This is consistent with the result of Cr-doped $BaTiO_3$ synthesized using a similar method.[5] When the size of $BaTiO_3$ becomes close to the critical size of 5 nm[20], the crystal structure is predominantly cubic phase, which makes it more difficult to probe the phase transition under different Mn doping concentration. The enlarged XRD pattern around 45 degrees of all three samples shows similar features. The relatively poor signal to noise ratio of the peak makes it difficult to observe minor change of the peak. However, some peak asymmetry is still observed, indicating possible cooperative tetragonal distortion.

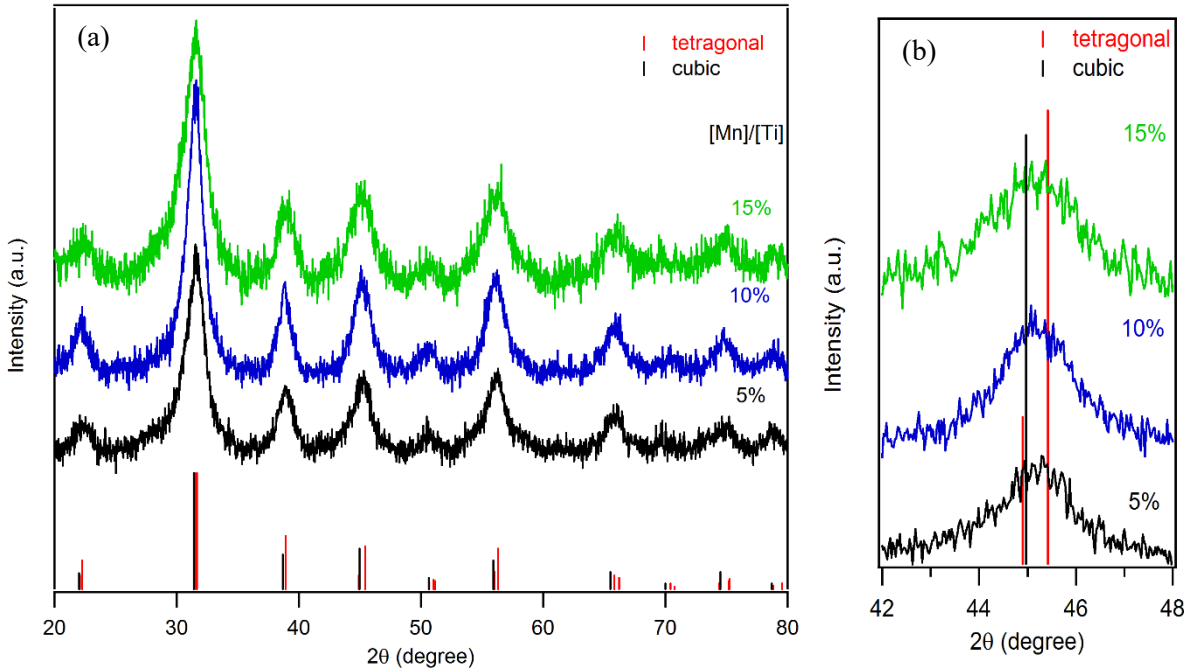

Figure 3-5: (a) XRD patterns of Mn-doped BaTiO3 samples synthesized in ethanol with different starting Mn/Ti ratio. The vertical lines correspond to the XRD patterns of bulk cubic (black) and tetragonal (red) $BaTiO_3$. (b) Enlarged XRD pattern around cubic (200) peak and tetragonal (200) and (002) peaks.

Raman spectroscopy has been used to further investigate the phase transition of Mn-doped $BaTiO_3$. As shown in Figure 3-6, the main bands centered at 180, 300, 520 and 719 cm^{-1} are attributed to [E(TO), A_1(TO)], [E(LO+TO), B_1], [E(TO), A_1(TO)] and [E(LO), A_1(LO)] modes, respectively. The spectrum of the 5% Mn doped sample has a weak peak around 300 cm^{-1} along with a very broad peak centered at 719 cm^{-1} which indicates the presence of local tetragonal structure in the sample. The 10% Mn doped samples have a similar spectrum suggesting the structure manintains some degree of teragonal distortion which is in agreement with the asymmetric peak observed in XRD. In the spectrum of the 15% Mn-doped sample, the peaks centered at 300 cm^{-1} and 720 cm^{-1} completely vanish and even the peak centered at 520 cm^{-1} is weaker than that of 5% and 10% doped samples which further confirms the structural transition into the cubic phase.

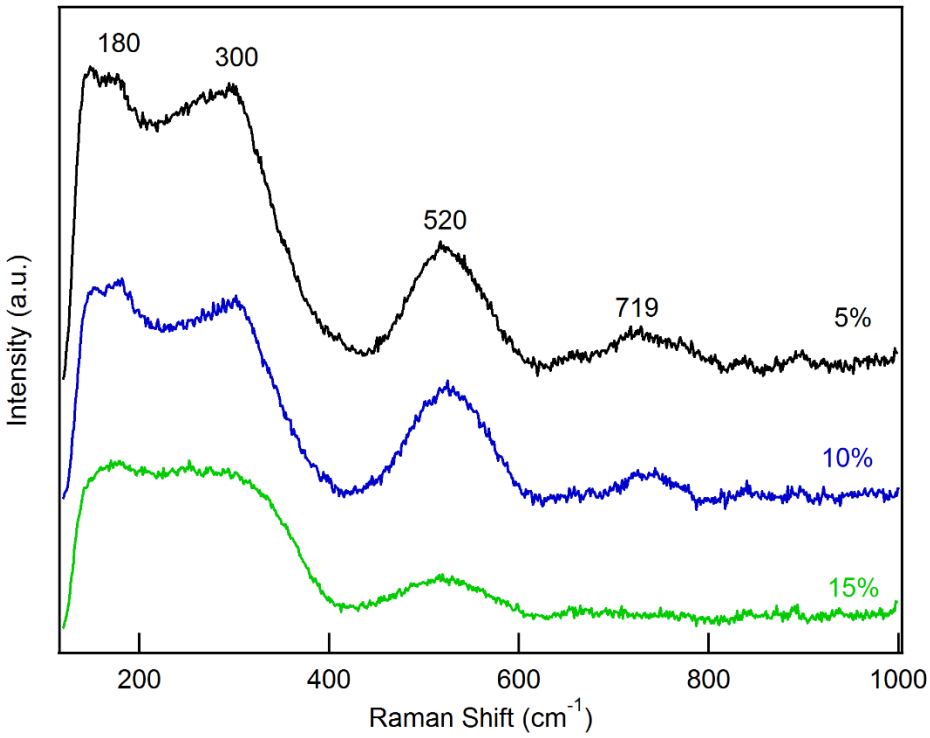

Figure 3-6: Raman spectra of Mn-doped BaTiO3 NPs prepared in ethanol with different starting Mn/Ti molar ratios of 5%, 10% and 15%.

3.5 UV-visible Absorption Spectrum

Figure 3-7 shows a typical electronic absorption spectrum of 10% Mn-doped $BaTiO_3$ synthesized in ethanol. The spectrum of a diluted colloidal suspension (red trace) clearly shows the band gap absorption of $BaTiO_3$. The calculated value of the band gap energy is 3.6 eV which is higher than the reported value for bulk $BaTiO_3$. Suzuki, K. and Kijima, K studied the optical band gap of pure $BaTiO_3$ with different sizes.[88] They found that when the particle size less than 11.5 nm, the band gap energy starts to increase and changes dramatically when the particle size is close to 7 nm. A small shoulder around 500 nm is observed in the spectrum of concentrated colloidal suspension which can be assigned to the ligand field transition of Mn^{3+}. In addition, Mn^{2+} (d^5) is silent in the ligand field spectroscopy. Although the Mn precursor is in the form of Mn^{2+},

the presence of Mn^{3+} is likely due to the oxidative reaction conditions. The coexistence of different oxidation states of Mn dopant ions has also been observed in Mn-doped SnO_2[89] and In_2O_3.[61]

In the Tanabe-Sugano diagram, the ground state term of high spin Mn^{3+} (d^4) ions is ^5D (Figure 3-7 Inset). In the ideal octahedral (O_h) symmetry, ^5D splits into a lower ^5E_g and a higher $^5T_{2g}$ term which gives the spin allowed transition $^5E_g \rightarrow {}^5T_{2g}$. In the tetragonally distorted octahedral site, $^5T_{2g}$ and ^5E_g terms further transform into additional terms ($^5B_{2g}$ and ^5E_g from $^5T_{2g}$, $^5A_{1g}$ and $^5B_{1g}$ from ^5E_g) resulting in extra low-energy absorption features.[90] The small shoulder around 500 nm can be assigned to the transition to unresolved $^5T_{2g}$ components.[91,92] It is worth mentioning that Mn^{3+} ions tend to prefer the centrosymmetric positions as its occupied 3d orbitals hinder the hybridization with O 2p orbitals. Given that the Jahn-Teller distortion associated with Mn^{3+} ions has been observed in many studies, it is likely that, in this study, Mn^{3+} ions sit in the local environment with D_{4h} symmetry.

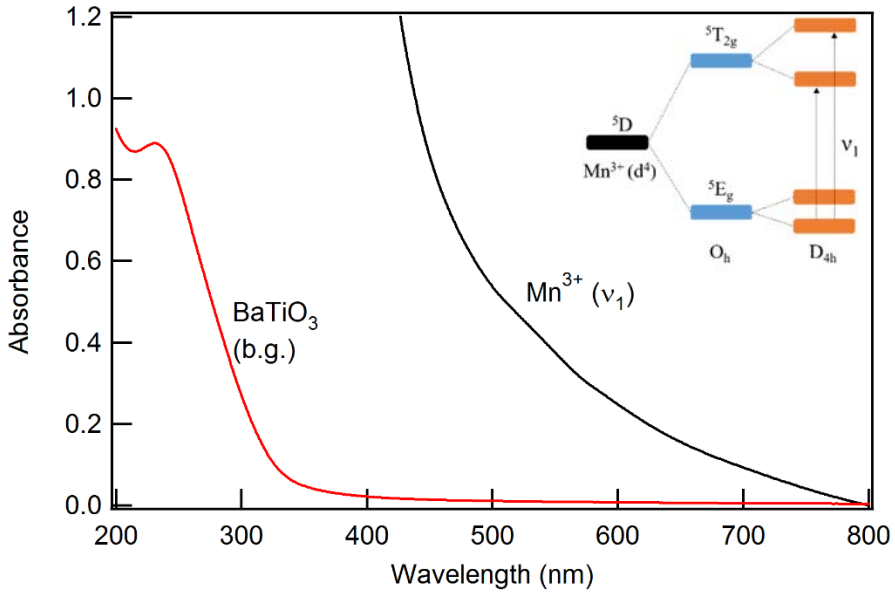

Figure 3-7: Typical UV-visible absorption spectrum (red) of colloidal Mn-doped $BaTiO_3$ NPs. The spectrum of concentrated samples (black) reveal the ligand field transition of Mn^{3+}. Inset: A schematic representation of the ligand field energy state splitting of Mn^{3+} in distorted octahedral sites.

3.6 X-ray Absorption Spectrum

The experimental recorded Mn L-edge X-ray absorption near-edge structure (XANES) spectrum (Figure 3-8 (a)) is compared with charge-transfer multiplet calculations (Figure 3-8 (b), (c) and (d)) using the CTM4XAS program.[93] The connection between crystal field theory and X-ray absorption spectra (XAS) was introduced in the work of de Groot *et al.*.[94] Figure 3-8 (c) and (d) shows the calculated XAS spectra of Mn^{2+} and Mn^{3+} ions in distorted octahedral sites with D_{4h} symmetry. The crystal field parameter 10Dq used in the calculation is 1.13 eV for Mn^{2+} and 2.30 eV for Mn^{3+}, which is in agreement with experimental values obtained from electron energy-loss spectroscopy (EELS) measurements.[95] The experimental XAS spectrum of 10% Mn-doped $BaTiO_3$ has a similar profile as the simulated spectrum for Mn^{2+} suggesting that the majority of Mn dopant exists as Mn^{2+} in the lattice. With careful inspection, around 648 eV and 652 eV, differences of detailed features can be found between the two spectra which could be related to the contribution of Mn^{3+} ions.

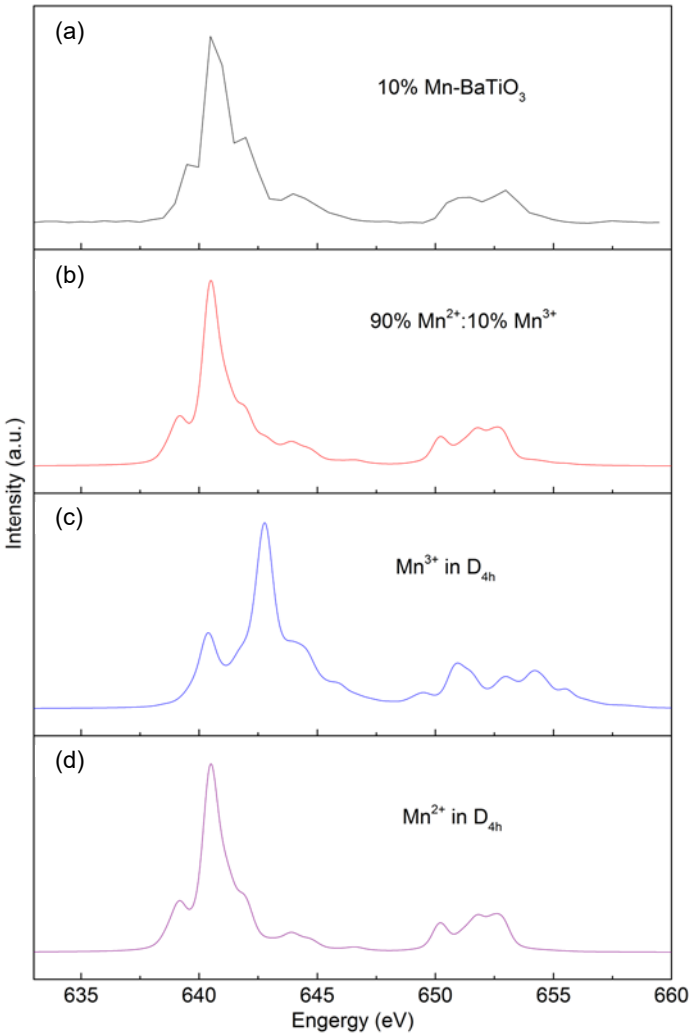

Figure 3-8: (a) Mn L-edge XAS spectrum of 10% Mn-doped $BaTiO_3$. (b) Linear combination of calculated XAS spectrum for Mn^{2+} (c) and Mn^{3+} (d).

Chapter 4 Synthesis of $BaTiO_3/CoFe_2O_4$ Composites

4.1 $BaTiO_3$ Building Blocks

As mentioned in previous chapters, nanoparticle size has a crucial effect on ferroelectric properties of $BaTiO_3$. In addition, morphology of the $BaTiO_3$ building block will affect interfacial contact with the magnetic component of the multiferroic composites which in turn will potentially affect the ME coupling between them due to the possible interfacial effect. $BaTiO_3$ NPs with larger size (BTO1) have been synthesized by modifying the method reported by Ju *et al.*[5] using water as a solvent. Small $BaTiO_3$ NPs (BTO2) were synthesized using the method proposed by Adireddy *et al.*[19]. Similar characterizations have been performed to investigate the crystal structure and morphology of the obtained samples.

Figure 4-1 shows XRD patterns of BTO1 and BTO2. Both patterns are in good agreement with the reference patterns, suggesting that synthesized samples have a perovskite structure. The minor peak around 24 degrees in BTO2 XRD pattern indicates the presence of a trace amount of $BaCO_3$ in the product which can be easily removed by washing with acetic acid.[96] Compared to the XRD pattern of BTO1, the XRD pattern of BTO2 shows a broadening of the peak along with a decrease in peak intensity suggesting a relatively smaller size of BTO2 nanostructures. Careful inspection of the region around 45 degrees shows the peak position of the BTO2 pattern slightly shifts towards the black line which corresponds to the cubic $BaTiO_3$ (200), indicating, to some degree, less tetragonality of the BTO2 sample compared to BTO1sample.

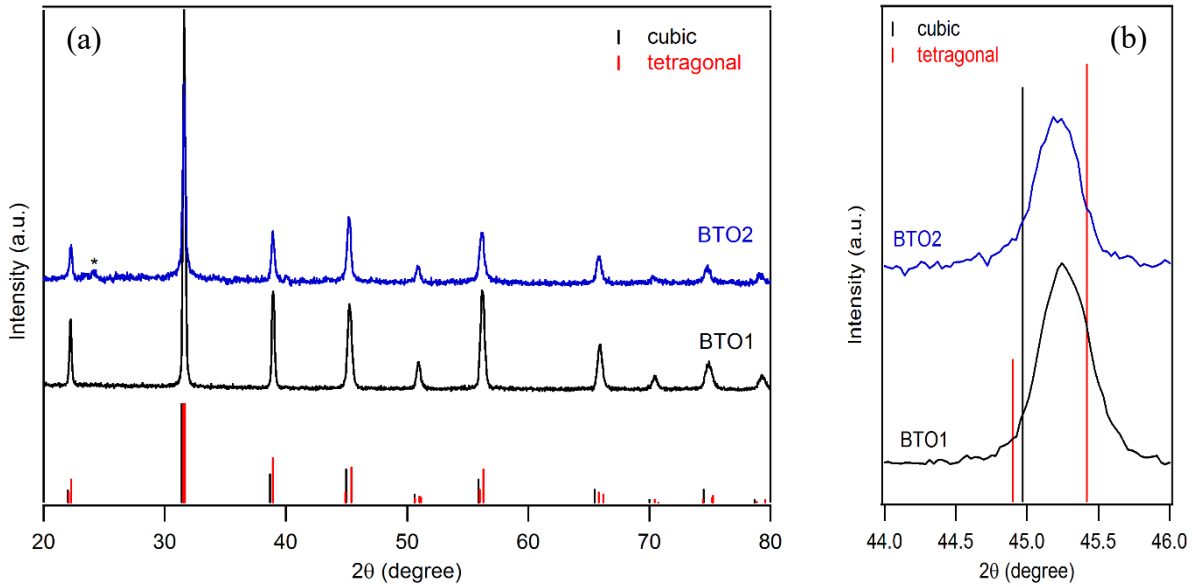

Figure 4-1: (a) XRD patterns of BTO1 and BTO2. The vertical lines correspond to XRD patterns of bulk cubic (black) and tetragonal (red) $BaTiO_3$. (b) Enlarged XRD pattern around cubic (200) peak (black line) and tetragonal (200) and (002) peaks (red lines).

The morphology of $BaTiO_3$ building blocks was investigated by TEM. BTO1 NPs have similar morphology compared to the previous literature report[5] which is confirmed by the TEM images of the composite containing the BTO1 building block (Figure 4-10). However, the morphology of the BTO2 sample is different from the reported cube-like morphology in the work of Adireddy *et al.*[19]. Figure 4-2 (a) shows the TEM overview image of the BTO2 sample. From the image we can see that the BTO2 sample consists of NPs with a size less than 5 nm along with large aggregates made of smaller NPs. It is worth mentioning that selected area electron diffraction (SAED) images (Figure 4-2(a) Inset) of the aggragate shows a single-crystalline feature which is not expected for randomly oriented NPs of this size. One of the possible explaination is that small NPs undergo an oriented attachment to form a larger aggregate which has been observed in hydrothermal synthesis of several oxides.[97,98,99] The HRTEM image shown in the inset of Figure 4-2(b) indicates separated small NCs with a size ca. 4 nm, which are single-crystalline. When the small NCs attache to each other, large domains are formed as shown in the image. Futhremore, the

large domains might stablize the tetragonal phase which is favorable for ferroelectric properties even though some local defects are observed in the image. These results suggest a promise of the $BaTiO_3$ NPs synthesized in solution as building blocks for functional ferroelectric and multiferroic nanostructures.

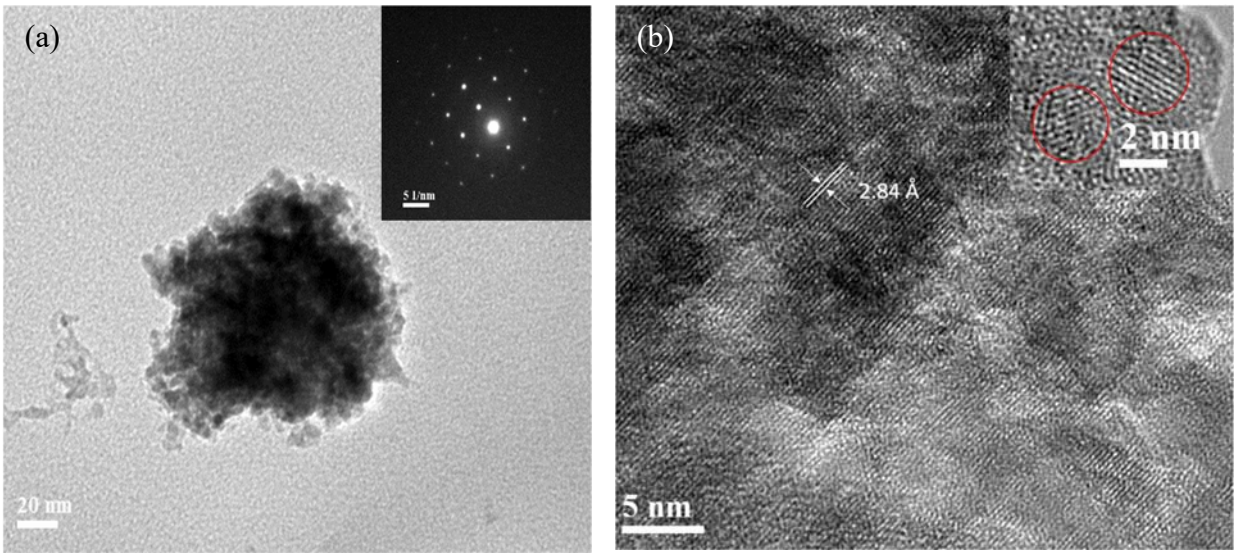

Figure 4-2: (a) Representative overview TEM image of BTO2 sample. Inset: SAED image of the aggregate shown in the image. (b) HRTEM image of BTO2 sample. Inset: HRTEM image of separated NPs.

The Raman spectra of both BTO1 and BTO2 are shown in Figure 4-3. The spectrum of commercial bulk $BaTiO_3$ is also collected as a reference for tetragonal $BaTiO_3$. The spectrum of as-synthesized BTO1 clearly shows peaks centered at 303 cm^{-1} and 716 cm^{-1}. Compared to the spectrum of bulk $BaTiO_3$, these characteristic peaks only exhibit minor weakening and broadening which indicates that BTO1 NPs are fully tetragonal. Even though the peak intensity decreases dramatically for the BTO2 sample, a small peak can still be observed at ca. 303 cm^{-1} (Figure 4-3 Inset). Together with the presence of a weak and broad peak around 716 cm^{-1}, the spectrum indicates that the BTO2 sample maintains some tetragonal distortion which is consistent with the above XRD and TEM results. Despite less tetragonality observed in the BTO2 sample, it could

still be a good candidate as a building block of multiferroic composites due to its large surface area.

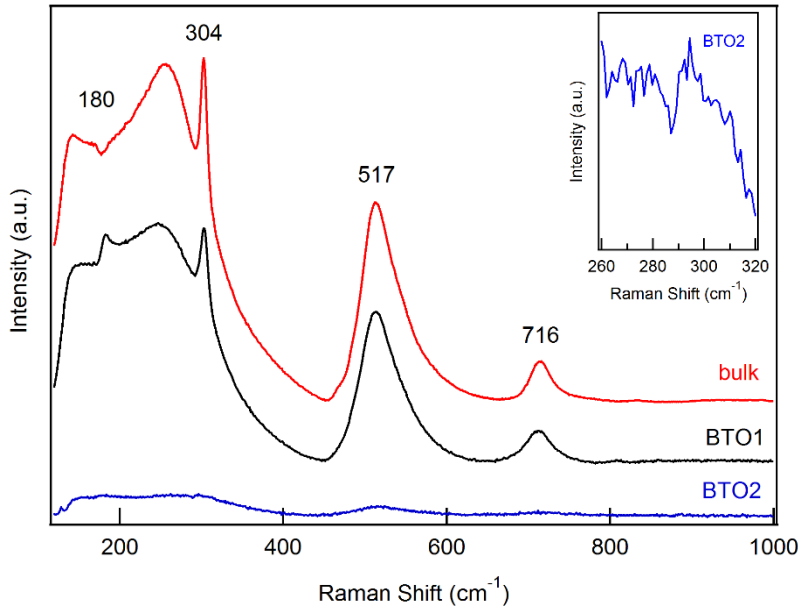

Figure 4-3: Raman spectra of BTO1, BTO2 samples and commercial bulk $BaTiO_3$. Inset: Enlarged spectrum around ca. 300 cm^{-1} region.

4.2 $Co_{0.6}Fe_{2.4}O_4$ Building Block

$CoFe_2O_4$ NPs with small average size were synthesized by the hydrothermal reaction reported by Li *et al.*[39] and incorporation into BTO1 NPs was attempted by impregnation. The XMCD results show that even the smallest stoichiometric $CoFe_2O_4$ NPs synthesized in this work exhibit at least some magnetic interaction at room temperature associated with Fe^{3+} ions (Appendix, FigrueA2). In addition, there is no noticeable XMCD signal in the Ti L-edge spectrum which might indicate that magnetic building blocks with stronger room-temperature magnetization are needed. As mentioned in chapter 1, both size and atomic ratio of Co to Fe of $CoFe_2O_4$ will affect its magnetic properties. Nonstoichiometric $Co_{0.6}Fe_{2.4}O_4$ (CFO) with larger size was synthesized using the method proposed by Wu *et al.*[100].

Figure 4-4 shows the XRD pattern of synthesized CFO sample. The diffraction peaks of the CFO sample are in agreement with the reference diffraction pattern for the inverse spinel structure of $CoFe_2O_4$, which clearly shows (220), (311), (222), (400), (422), (511) and (440) diffraction peaks. Estimated particle sizes calculated using the Debye-Scherrer equation were ca. 20 nm. The main reason for the relatively low signal to noise ratio in the XRD pattern is that Co and Fe strongly fluoresce with the copper radiation wavelength (λ = 1.5406 Å), which was used as the X-ray source in these measurements.

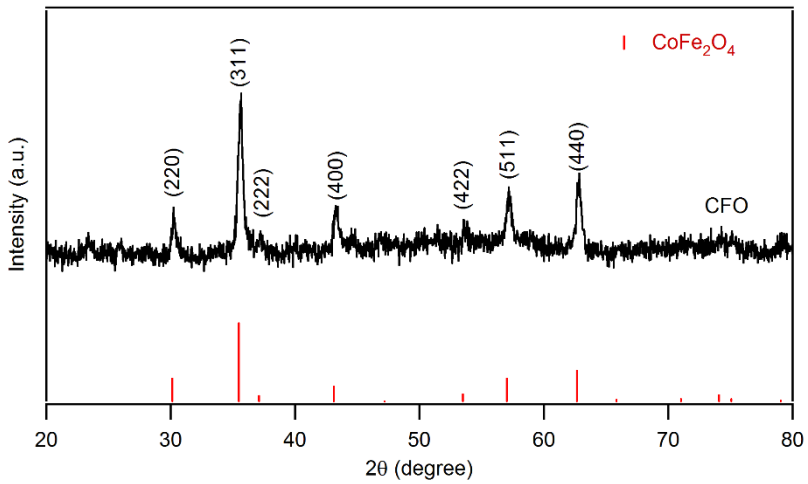

Figure 4-4: Representative XRD pattern of CFO sample. The vertical line corresponds to the XRD pattern of bulk $CoFe_2O_4$ (JCPDS no. 22-1086).

Figure 4-5 (a) shows the TEM image of a synthesized CFO sample deposited on carbon-coated Cu grids. These NPs have a cubic morphology with a relatively narrow size distribution. The average particle size is measured to be ca. 22.5 nm which is consistent with the value calculated from XRD measurements. The NC sizes of these samples were consistently measured for the longest edges, and the average size was determined as an ordinary arithmetic mean (number average). The HRTEM image of single CFO NCs reveals the single crystalline nature of these nanocubes (Figure 4-5 (a) Inset). The lattice spacing measured from the inset is 2.95 Å, which corresponds to the lattice spacing of the (220) plane of inverse spinel $CoFe_2O_4$ (2.96 Å). The EDX

results confirmed that synthesized NCs contain both Co and Fe with an atomic ratio (8.13 : 40.12) slightly less than to that of $Co_{0.6}Fe_{2.4}O_4$.

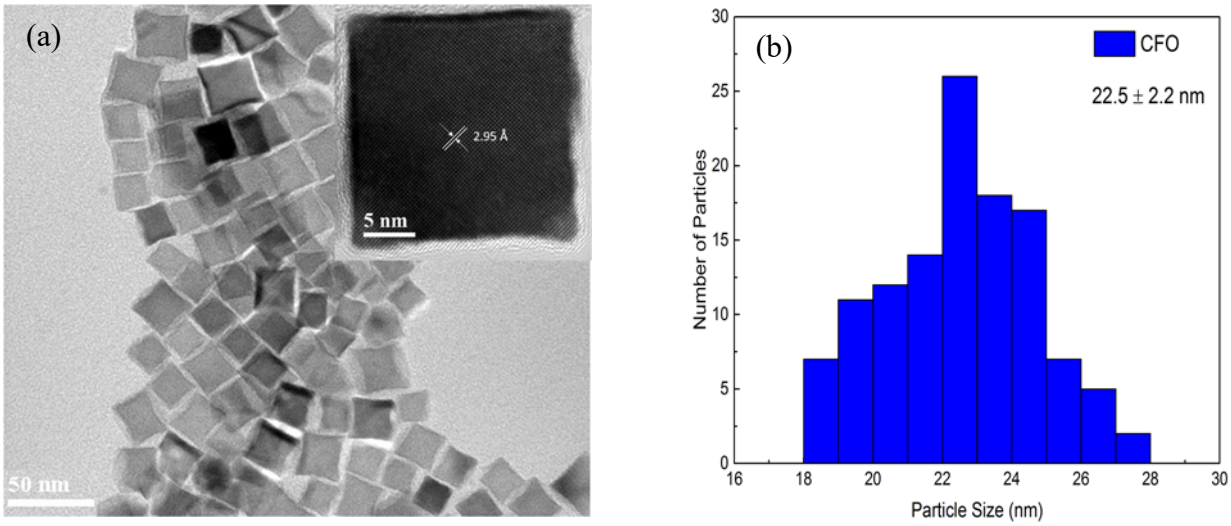

Figure 4-5: (a) Representative TEM image of CFO sample. Inset: HRTEM image of a single nanocrystal. (b) Size distribution histogram of CFO NCs.

$CoFe_2O_4$ has an inverse spinel structure with ideal cubic symmetry ($Fd\bar{3}m$), which gives rise to 39 phonon modes.[101] Among them, five modes ($A_{1g} + E_g + 3T_{2g}$) are Raman active.[102] With cation redistribution, which usually happens in spinel ferrites, the symmetry of the crystal structure is altered resulting in more Raman active modes. For instance, 6 phonon modes were observed in Raman spectrum of tetragonal $CoFe_2O_4$.[103] Raman spectra of a typical CFO sample synthesized in this work is shown in Figure 4-6. The spectrum clearly shows four peaks with the maxima at 186, 311, 470, and 680 cm^{-1}. According to literature[104], the phonon mode with frequency higher than 600 cm^{-1} can be assigned to the A_{1g} symmetry involving symmetric stretching of O atoms with respect to central metal ions located in tetrahedral sites. The low-frequency phonon modes, E_g and T_{2g}, are related to the M-O (metal-oxygen) bond bending around the metal ions in the octahedral site. In addition, the peak centered at 470 cm^{-1}, T_{2g}, is usually observed at the same positions in the Raman spectrum of $CoFe_2O_4$. This band is solely contributed by Co^{2+} ions in the octahedral

site. Reported peak position of A_{1g} varies from 695 cm^{-1} for bulk $CoFe_2O_4$ to 675 cm^{-1} for 6 nm $CoFe_2O_4$ NPs due to the ion distribution accompanying the size change.[104] The peak located at 680 cm^{-1} is observed for synthesized CFO sample which could be attributed to the relatively small size of the NCs. The Raman signal between 500 and 650 cm^{-1} is likely to come from the unresolved A_{1g} and T_{2g} peak given its low signal to noise ratio.

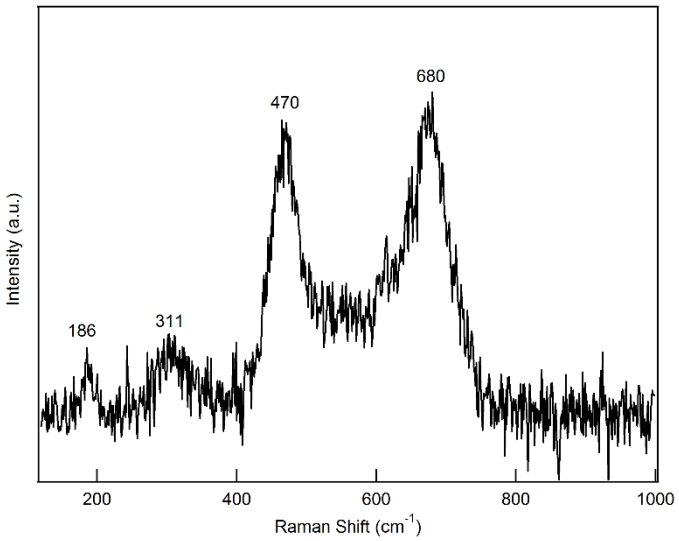

Figure 4-6: Raman spectrum of synthesized CFO sample.

The UV-visible absorption spectrum of a synthesized CFO sample is shown in Figure 4-7. The crystal field d-d transition of cobalt ferrite is focused on the Co^{2+} ions in the lattice as Fe^{3+} ions with d^5 is spectroscopically silent. The enlarged spectrum (Inset) shows a small shoulder around 480 nm which corresponds to the $^4T_1(F) \rightarrow {}^4T_1(P)$ crystal field transition of Co^{2+} in octahedral sites. This peak was observed in Co^{2+} doped MgO with a relatively low intensity as it is electric dipole forbidden.[105] In the case of $CoFe_2O_4$ with ion redistribution, a d-d transition of Co^{2+} in tetrahedral sites ($^4A_2 \rightarrow {}^4T_1(P)$) is usually observed around 600 nm.[106] The peak is not clearly shown in this spectrum probably due to the lower atomic ratio of Co^{2+} ions in the lattice resulting in much less Co^{2+} redistributed to tetrahedral sites. According to the literature[107,108,109], the shoulder around 340 nm can be assigned to the metal-metal charge transfer between

octahedrally coordinated Co^{2+} and Fe^{3+} ($[Co^{2+}]t_{2g} \rightarrow [Fe^{3+}]e_g$). The sharp increase of absorbance around 300 nm can be attributed to the charge transfer between Fe^{3+} ions located on different crystallographic sites ($(Fe^{3+})t_2 \rightarrow [Fe^{3+}]e_g$).

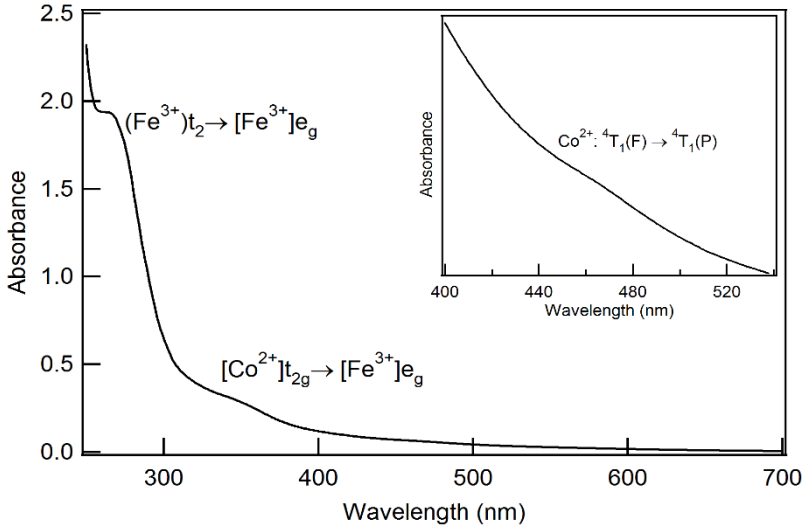

Figure 4-7: Representative UV-visible absorption spectrum of CFO NCs. (Note that the parentheses denote tetrahedral coordination and square brackets denote octahedral coordination.) Inset: Enlarged spectrum at 400-540 nm region.

The magnetic properties of as-synthesized CFO NCs were measured by PPMS. Figure 4-7 shows the room-temperature magnetic hysteresis of a nonstoichiometric CFO sample. The saturation magnetization is about 50 emu/g, which is in agreement with a corresponding value reported in the literature.[100] The coercivity of the sample is 1368 Oe, which is slightly larger than the reported value. This could be attributed to a larger average particle size of our NCs.

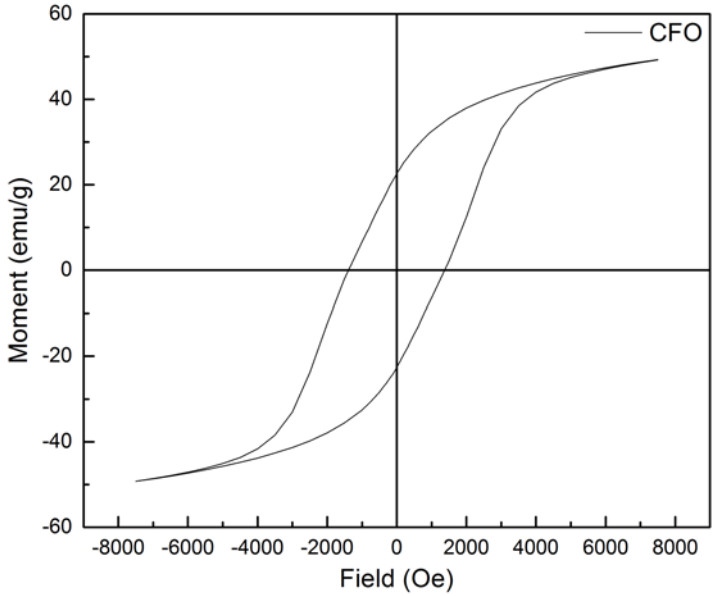

Figure 4-8: Magnetic hysteresis loop of synthesized CFO sample measured at room temperature.

4.3 CFO-BTO Composites

The BTO samples described above offer some unique opportunities as building blocks for multiferroic materials. With the ferroelectric and ferrimagnetic building blocks mentioned above, two different methods were applied to obtain composites based on particle size and morphology. Providing that possible hollow structure of BTO1 building blocks, impregnation method was attempted to incorporate smaller CFO building blocks into large BTO1 NPs to obtain analogous core-shell type CFO-BTO1 composite. The BTO2 sample with small particle size and oriented attachment characteristics was combined with CFO NCs using spin-coating to form a multi-layer structure CFO-BTO2 composite.

The XRD pattern of obtained CFO-BTO1 composite is shown in Figure 4-9 panel (a). The XRD pattern clearly shows diffraction peaks corresponding to both the BTO and CFO phases. Compared to the XRD patterns of pure CFO and BTO1 sample, the ratio of the peak intensity of CFO (311) to BTO1 (101) is greater than the ratio of those two peaks in the XRD pattern of the

composite, which indicates the composite contains relatively small amounts of CFO compared to BTO1. Panel (b) shows the XRD pattern of a CFO-BTO2 thin film on a sapphire substrate. The poor signal to noise ratio is due to the small amount of sample on the substrate (1.2 mg in total). The pattern shows diffraction peaks that belong to BTO2 and CFO phases. A systematic shift of peak positions is observed compared to those of pure CFO and BTO2. The reason is likely to be the offset of the height of the thin film surface with respect to the incident X-ray. In another aspect, the peak intensity of CFO (311) to BTO2 (101) is close to the ratio of these two peaks in the XRD pattern CFO-BTO2 thin film, which suggests more CFO NCs are incorporated into the multi-layer structure, compared to the CFO-BTO1 composite obtained by the impregnation method. Thus the multilayer CFO-BTO2 thin film structure has a higher loading of CFO building blocks.

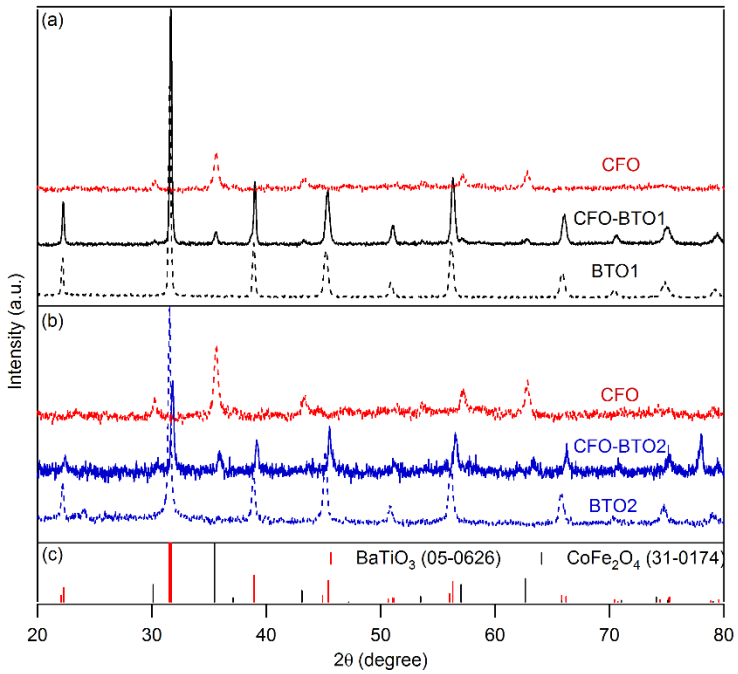

Figure 4-9: XRD patterns of composites obtained by impregnation (a) and spin coating (b). The dash lines correspond to XRD patterns of respective building blocks. The vertical lines in (c) represent the XRD pattern of bulk $BaTiO_3$ (red) and $CoFe_2O_4$ (black).

The morphology of obtained composites was confirmed with TEM. Figure 4-10 (a) shows the overview image of a CFO-BTO1 composite in which some small CFO nanocubes are located

on the surface of the large BTO1 NPs. In addition, some small NPs with cube-like morphology can be found inside larger BTO1 NPs, which indicates some CFO NCs incorporate into the interior of BTO1 NPs. The HRTEM images ((b) and (c)) taken from different locations show the crystalline structures with lattice spacing of 2.83 Å and 2.93 Å which correspond to $BaTiO_3$ (110) and CFO (220), respectively. Figure 4-10 (d) shows a TEM image of fragments of a CFO-BTO2 thin film obtained by sonicating thin film sample in ethanol and then depositing onto a carbon-coated Cu grid. From the image, we can see that the CFO NCs are embedded into the large chunk formed by the aggregation of small BTO2 NPs. The corresponding HRTEM image (Figure 4-10 (e)) clearly shows the lattice spacing characteristic for CFO (2.93 Å) and BTO2 (2.85 Å) building blocks.

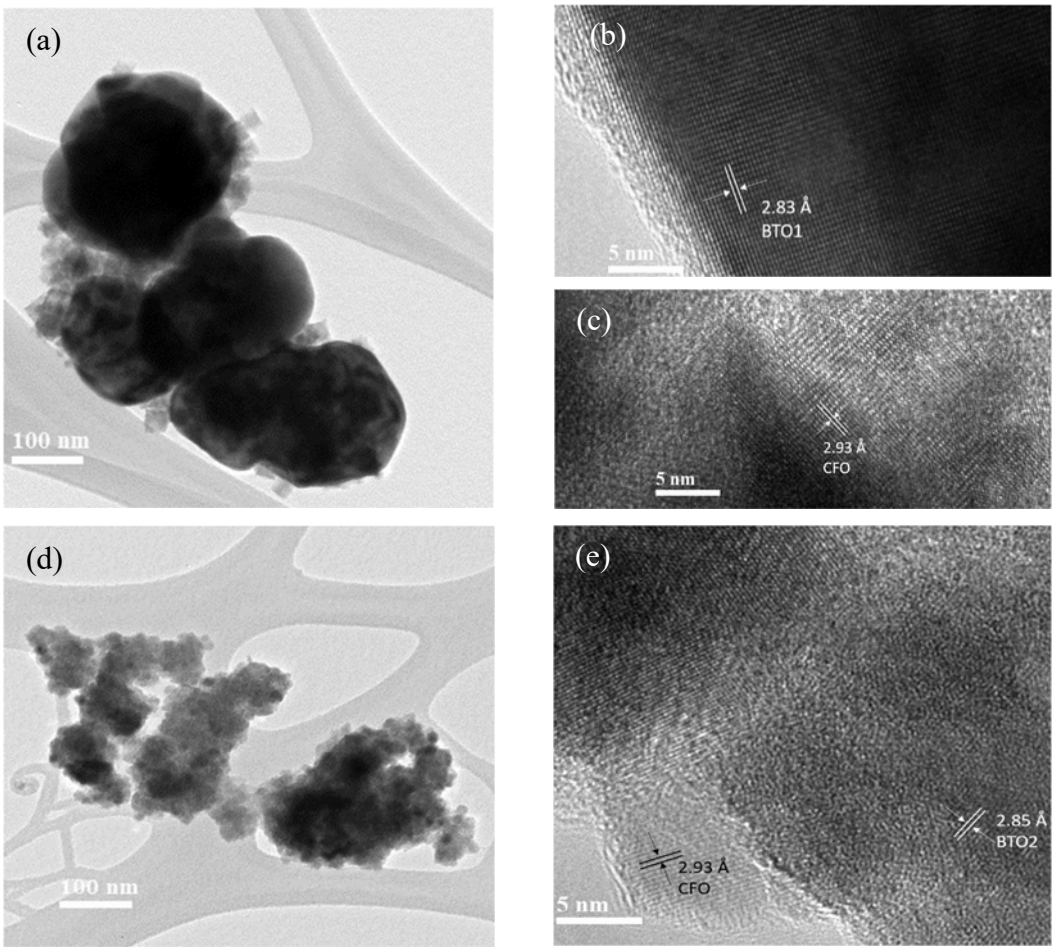

Figure 4-10: TEM images of the composites obtained by impregnation (a) and spin coating (d). (b) and (c) HRTEM images from different spots on image(a). (e) HRTEM image of CFO-BTO2 thin film sample.

Mild annealing was applied to form an effective interface between two building blocks during sample preparation. Raman spectroscopy was used to confirm the crystal phase of the $BaTiO_3$ component within the heterostructure. Figure 4-11 (a) shows a Raman spectrum of the CFO-BTO1 composite. The sharp peak centered at ca. 303 cm^{-1} along with the broad peak at around 716 cm^{-1} confirm that the composite maintains a large degree of tetragonality after annealing at 273 K. Compared to the Raman spectra of the BTO1 and CFO building blocks, the profile of the composite is similar to that of BTO1, suggesting a large amount of BTO1 in the heterostructure. The asymmetric feature of both peaks at around 520 and 716 cm^{-1} can be attributed to the contribution of the CFO Raman peak which confirms the presence of CFO NCs in the

composite. The Raman spectrum of a CFO-BTO2 thin film (Figure 4-11 (b)) shows a small sharp peak around 300 cm^{-1} which is consistent with the spectrum of BTO2. Compared to the Raman spectra of CFO and BTO2, at energies below 400 cm^{-1}, the spectrum of CFO-BTO2 heterostructure is comparable to that of BTO2. While, after 400 cm^{-1}, the spectrum of the composite consists primarily CFO Raman peaks with a large contribution of BTO Raman peak around 520 cm^{-1}. It suggests that the CFO-BTO2 thin film has a higher percentage of CFO building bocks compared to that of the CFO-BTO1 heterostructure which agrees well with XRD results.

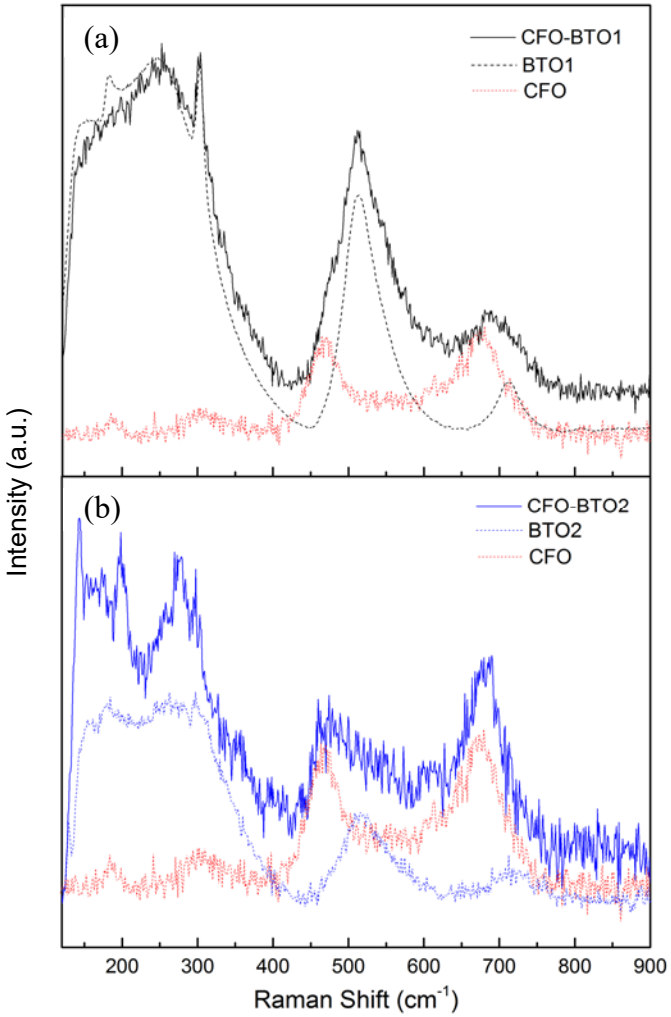

Figure 4-11: Raman spectra of the composite prepared with impregnation (a) and spin coating (b) method. The traces with dash line are Raman spectra of corresponding build blocks.

Figure 4-12 shows magnetic hysteresis loops collected at different temperatures for the composites prepared using (a) impregnation and (b) spin coating. Similar to other magnetic materials, both coercivity and saturation magnetization of the composites increase with decreasing temperature. The flat red dashed line, that is indistinguishable from the baseline, in both Figure4-12 (a) and (b) confirms that BTO1 and BTO2 components have no contribution to the net magnetization. A difference in the magnetic moment of the two heterostructures is mainly caused by the large difference of sample mass. At 300K, the coercivity of both composites is slightly larger than the value reported in the literature, which can possibly be attributed to the elimination of defects during the annealing process.[100] Importantly, this work demonstrates that configuration and interfaces in composite materials containing rationally chosen magnetic and ferroelectric components can be designed by varying the nanostructure morphology, composition, and surface area. The results reported in this Chapter represent a new building block approach to multiferroic nanostructures as an alternative to top-down, gas phase, or typical solid state approaches.

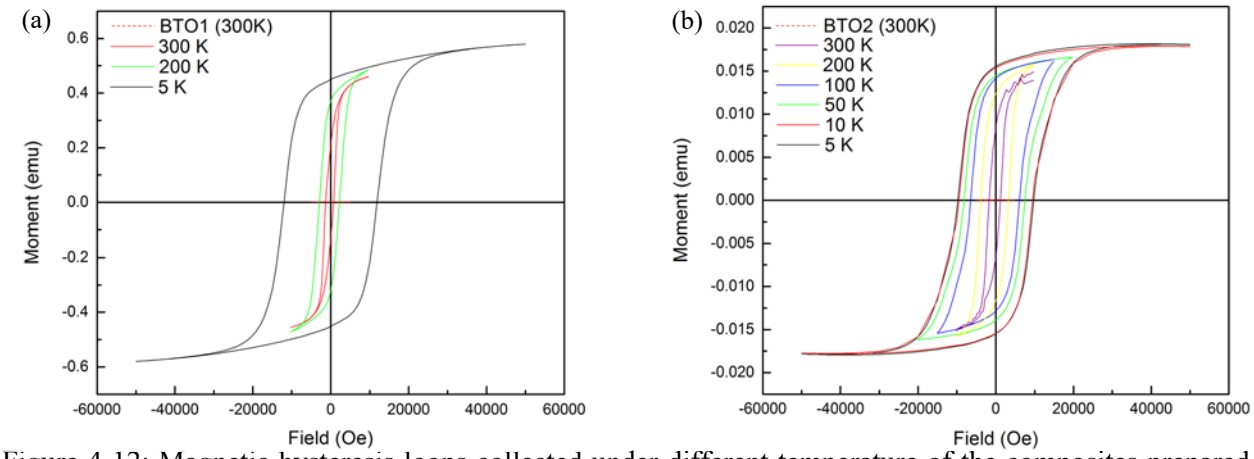

Figure 4-12: Magnetic hysteresis loops collected under different temperature of the composites prepared by impregnation (a) and spin coating (b).

Chapter 5 Synthesis of $Co_{0.6}Fe_{2.4}O_4$-$PbTiO_3$ Composite

5.1 $PbTiO_3$ Thin Films

As mentioned in chapter one, compared to $BaTiO_3$, $PbTiO_3$ has a higher net spontaneous polarization and T_C, which makes it more favorable in terms of practical application and device fabrication. Transparent $PbTiO_3$ thin films were obtained by spin-coating a suspension of amorphous NPs followed by annealing at 773 K. The obtained $PbTiO_3$ thin film can be incorporated with $Co_{0.6}Fe_{2.4}O_6$ NCs to make a transparent multi-layer heterostructure which is compatible for interesting spectroscopic studies and device fabrication.

The XRD patterns of as-synthesized amorphous NPs and annealed samples are shown in Figure 5-1. The as-synthesized NPs are amorphous as confirmed by the XRD pattern with only one broad peak observed. After annealing at 773 K, the amorphous NPs turn into crystalline tetragonal $PbTiO_3$ as its XRD pattern (black trace) is in a good agreement with that of bulk tetragonal $PbTiO_3$. Unlike $BaTiO_3$, $PbTiO_3$ has a distinguishable XRD pattern between cubic and tetragonal phases. Especially, the highest-intensity peak (31.95°) of the cubic phase (110) splits into the highest- (31.48°) and second highest-intensity peaks (32.46°) of tetragonal (101) and (110) which can be used to unambiguously differentiate between the cubic and tetragonal phase of $PbTiO_3$. It is worth mentioning that annealing temperature is slightly higher than T_C of $PbTiO_3$ (763 K). The annealed sample still keeps its tetragonal phase due to the reversible phase transformation of $PbTiO_3$, for which high-temperature cubic phase will convert to tetragonal phase spontaneously when temperature is below T_C.[26] The XRD pattern of an annealed thin film on a quartz substrate has a relatively low peak intensity because of the small amount of sample on the substrate. However, after careful inspection, one still can observe split peaks around 32 degrees (Figure 5-1 Inset) along with the peaks located at the positions corresponding to diffraction peaks

of tetragonal lead titanate which indicates that annealed thin films have a perovskite structure with significant tetragonal distortion. The impurity peak located at around 30 degrees could be attributed to pyrochlore $Pb_2Ti_2O_6$ which has been observed as an intermediate in the transformation from amorphous to tetragonal $PbTiO_3$ with annealing.[110,111] This pyrochlore phase can be removed by further annealing at higher temperature.[112]

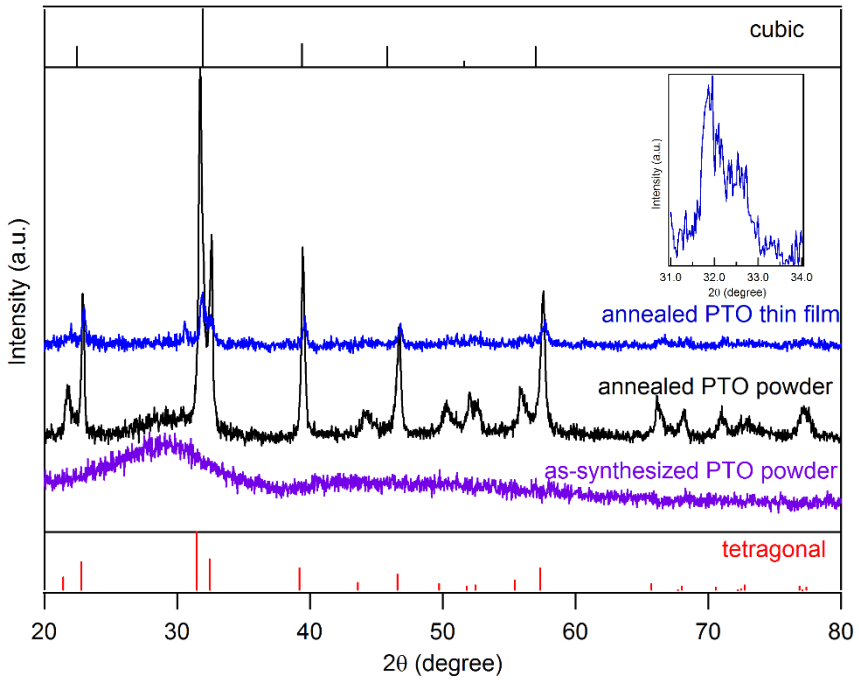

Figure 5-1: XRD patterns of as-synthesized NPs with (black) and without annealing (purple) and annealed $PbTiO_3$ thin film (blue). Inset: Enlarged XRD pattern of annealed thin film at the region around tetragonal $PbTiO_3$ (101) and (110) diffraction peaks. The vertical lines represent of bulk tetragonal (red, JCPDS no. 06-0452) and cubic (black, JCPDS no. 40-0099) $PbTiO_3$.

The morphology of the obtained $PbTiO_3$ thin film was obtained using SEM. Figure 5-2 (a) shows the low-magnification SEM image of the thin film. The annealed thin film has a relatively smooth surface without cracks observed at the 10-μm scale. In addition, the large bright spots on the surface correspond to large agglomerates made of small NPs as shown in the SEM image with a higher magnification (Figure 5-2 (b)). The formation of large agglomerates is favorable for the

stability of the tetragonal phase of $PbTiO_3$ in the thin film which supports the conclusion obtained from XRD measurement.

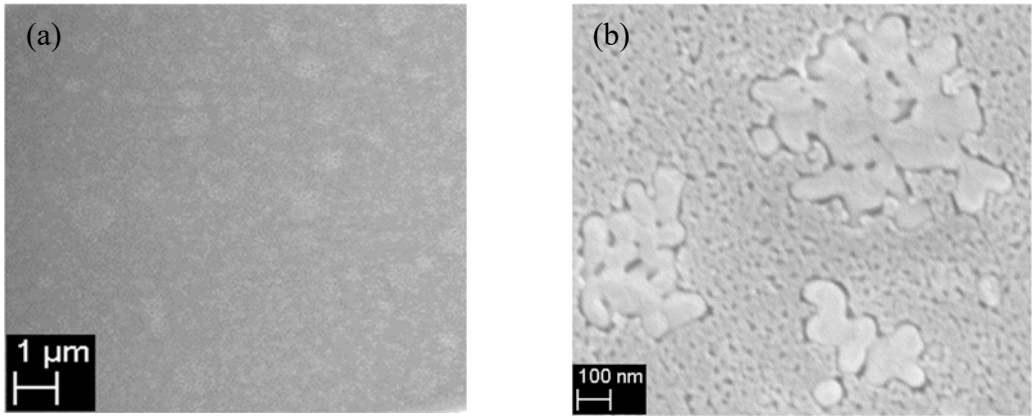

Figure 5-2: Low (a) and high (b) magnification SEM images of anneled $PbTiO_3$ thin film.

Cubic phase of $PbTiO_3$ with ideal O_h symmetry has 12 Raman-inactive phonon modes. With a distortion in the lattice of tetragonal $PbTiO_3$, these phonon modes further transform as $3A_1 + 4E + B_1$ which are all Raman active. Furthermore, all A_1 and E modes split to TO (transverse optical) and LO (longitudinal optical) components by a long range Coulomb force when propagating along symmetry axes.[76] All the above phonon modes of the tetragonal phase have been observed in the Raman spectrum of $PbTiO_3$ single crystal in the work of Burns and Scott.[113] It was also reported Raman peaks of tetragonal $PbTiO_3$ single crystal will shift towards lower wavenumber and become broad when the temperature approaches T_C, and eventually completely vanish after the structure transforms into the cubic phase.[114,115] Similar observations were also found in the case of polycrystalline $PbTiO_3$ thin films[116] and single crystalline nanowires (NWs)[117]. Figure 5-3 shows the Raman spectra of an annealed powder and thin film samples with and without annealing. The Raman spectrum of annealed powder sample clearly shows peaks centred at 147, 208, 287, 502, 612, and 716 cm^{-1}, which is in good agreement with peak positions reported for bulk $PbTiO_3$[112]. The assignments of Raman peaks to their corresponding phonon modes are indicated at the top of Figure 5-3. As expected, there is no Raman peak present in the spectrum of

a thin film made of amorphous NPs without annealing. After annealing, the spectrum of the thin film sample is very similar to the spectrum of annealed powder suggesting the thin film transformed into a tetragonal perovskite structure.

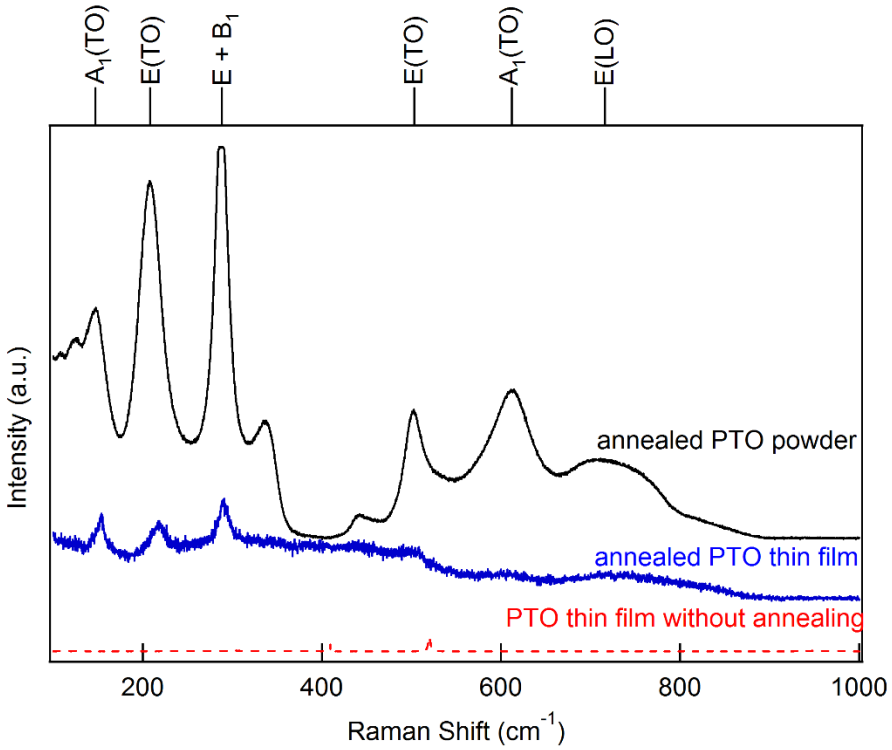

Figure 5-3: Raman spectra of the annealed powder (black) and thin film(blue). The red dash line is Raman spectrum of the thin film without annealing. The assignments of the Raman modes are indicated at the top of the graph.

Figure 5-4 shows the UV-visible absorption spectrum of the obtained transparent $PbTiO_3$ thin film as shown in the photograph (Figure 5-4 Inset). As evidence for the inset, the films are fully transparent, rending their compatibility with optoelectronic structure and devices. A sharp increase in absorbance starts from 365 nm corresponding to the band gap absorption of $PbTiO_3$. The band gap energy of the obtained thin film sample is estimated to be 3.4 eV which is consistent with the reported band gap energy for bulk $PbTiO_3$. In addition, the value is close to the reported band gap energy of 3.45 eV and 3.6 eV for $PbTiO_3$ NPs prepared by a sol-gel method[118] and $PbTiO_3$ thin films prepared using metalorganic chemical vapor deposition[119], respectively.

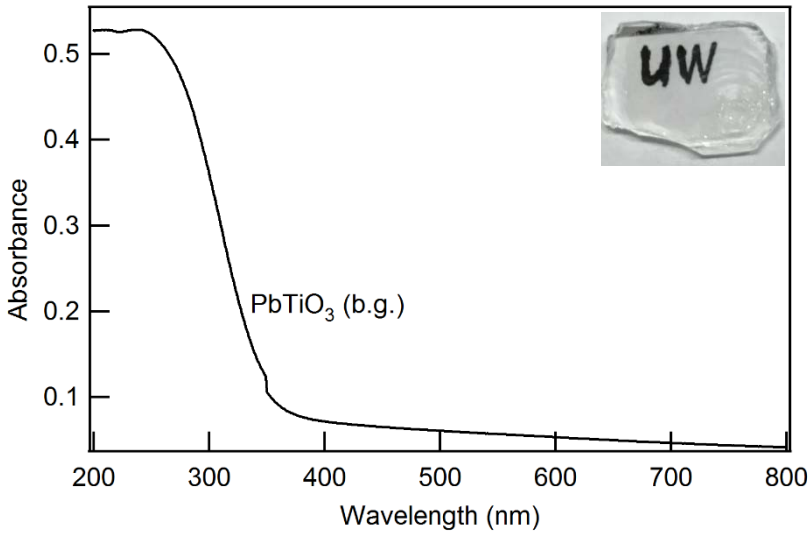

Figure 5-4: UV-visible absorption spectrum of obtained $PbTiO_3$ thin film. Inset: Photograph of the thin film.

5.2 $Co_{0.6}Fe_{2.4}O_4$-$PbTiO_3$ Multilayer Structure

A $Co_{0.6}Fe_{2.4}O_4$-$PbTiO_3$ (CFO-PTO) multilayer structure was prepared by spin coating a $Co_{0.6}Fe_{2.4}O_4$ NC suspension on top of the obtained $PbTiO_3$ thin film and annealing at 573 K to form an effective interface between the two building blocks. Figure 5-5 shows TEM images of a fragment of the CFO-PTO thin film obtained by sonicating the thin film and then depositing on a carbon coated Cu grid. The overview TEM image (Figure 5-5 (a)) shows a fragment of a $PbTiO_3$ thin film with some cube-like NCs at the top which suggests a heterostructure containing both building blocks was obtained. In addition, the EDX elemental maps obtained in STEM modes (Appendix, Figure A3) shows all elements, including Co, Fe, Ba, Ti, and O, evenly distributed across the thin film. A multi-domain structure can be seen in HRTEM image (Figure 5-5 (b)) of the heterostructure in which two domains with lattice spacing of 2.40 Å and 2.74 Å corresponds to $CoFe_2O_4$ (222) and $PbTiO_3$ (110), respectively. It is worth mentioning that the interface between the two building blocks can be clearly observed in the HRTEM image which provides us the ability to address the possible interfacial effect of the magneto-electric coupling between the ferroelectric

and ferrimagnetic component using XMCD combined with STXM (scanning transmission X-ray microscopy).

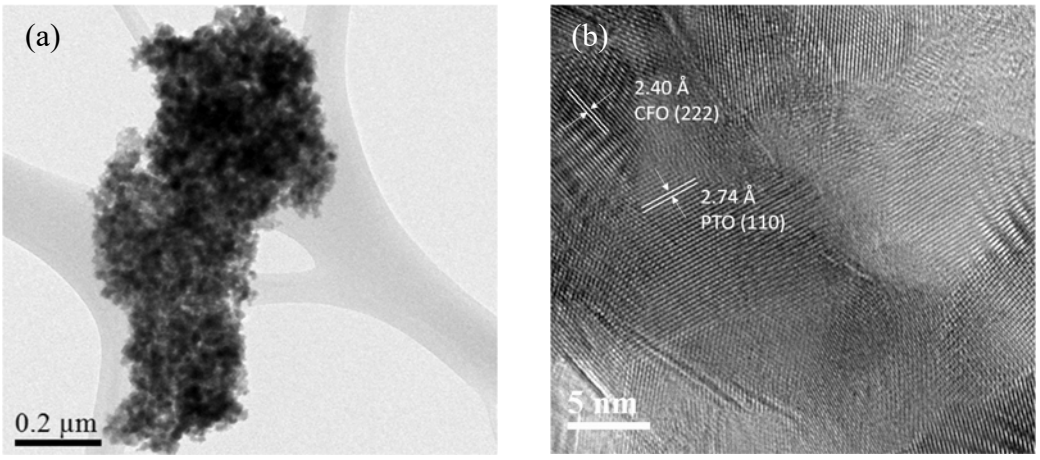

Figure 5- 5: Low magnification (a) and high resolution (b) TEM images of obtained $PbTiO_3$ thin film.

Figure 5-6 shows Raman spectrum of a CFO-PTO thin film. As expected, for $PbTiO_3$ component, the Raman peak intensity and peak position do not change after annealing at 573 K compared to that of a $PbTiO_3$ thin film. The Raman peaks of $Co_{0.6}Fe_{2.4}O_4$ are not well-resolved in the Raman spectrum of the CFO-PTO sample due to the low signal to noise ratio and relatively small amount of $Co_{0.6}Fe_{2.4}O_4$ in the heterostructure compared to $PbTiO_3$. However, there is a small

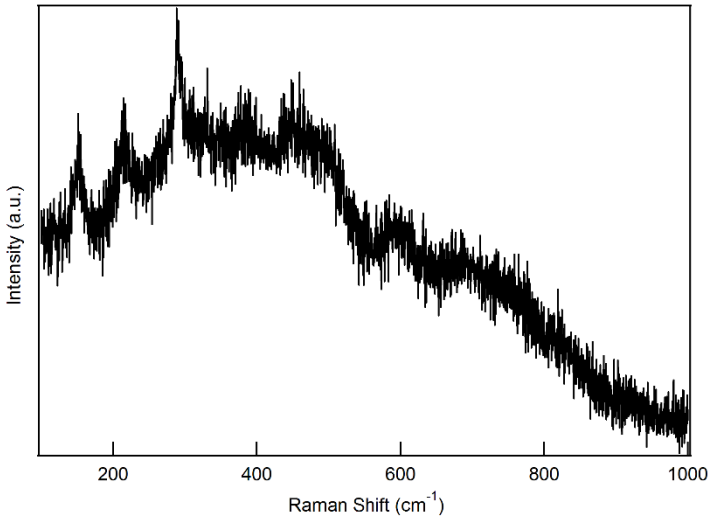

Figure 5- 6: Raman spectrum of CFO-PTO thin film.

difference between Raman spectrum of CFO-PTO and that of $PbTiO_3$ thin film in the range of 400-800 cm^{-1} which could possibly be related to the phonon modes of $Co_{0.6}Fe_{2.4}O_4$.

A UV-visible absorption spectrum for a transparent CFO-PTO thin film is shown in Figure 5-7. Compared to the absorption spectrum of a $PbTiO_3$ thin film, the increase of absorption between 380 to 800 nm could be attributed to the $Co_{0.6}Fe_{2.4}O_4$ NCs incorporated into the heterostructure. With careful inspection, a small shoulder around 480 nm can be observed which could be related to crystal field d-d transition of Co^{2+} ions located in octahedral sites. A similar shoulder has been observed in the optical absorption spectrum of a $Co_{0.6}Fe_{2.4}O_4$ NC suspension as mentioned in chapter 4. For wavelength of incident light less than 350 nm, band gap absorption of $PbTiO_3$ becomes dominant as the absorption spectrum of the CFO-PTO composite approaches to that of a $PbTiO_3$ thin film. The fully transparent CFO-PTO thin film provides an opportunity to use optical and magneto-optical spectroscopies to study the ME coupling between two building blocks by monitoring the behavior of bandgap absorption of $PbTiO_3$ under external magnetic field.

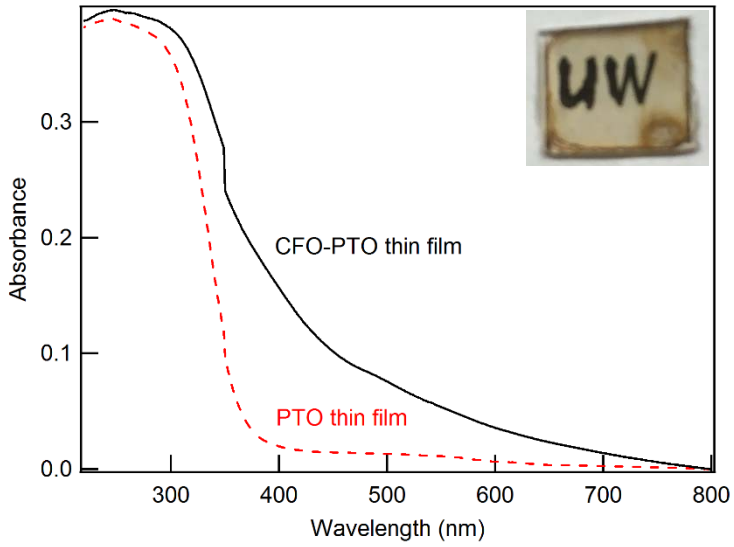

Figure 5-7: UV-visible absorption spectrum of CFO-PTO thin film (black) and PbTiO3 thin film as comparison (red dash line).

5.3 Alternative $PbTiO_3$ Nanostructure

One dimensional $PbTiO_3$ nanostructures could be an interesting alternative as a building block for multiferroic materials due to their anisotropic properties. $PbTiO_3$ nanoribbons have been synthesized by modifying the method proposed by Hu *et al.*[72]. In the hydrothermal synthesis of a perovskite material, the amount of mineralizer (KOH or NaOH) affects the morphology of the obtained product.[120] Similarly, the amount of NaOH used in this reaction also has an effect on the obtained $PbTiO_3$ nanostructures. Figure 5-8 shows the XRD patterns of obtained products that were synthesized with different amount of NaOH. Both XRD patterns are in good agreement with the XRD pattern of bulk tetragonal $PbTiO_3$. Compared to the XRD pattern of the sample synthesized with 10 mmol NaOH, diffraction peaks of the sample synthesized with 20 mmol NaOH has a much weaker peak intensity.

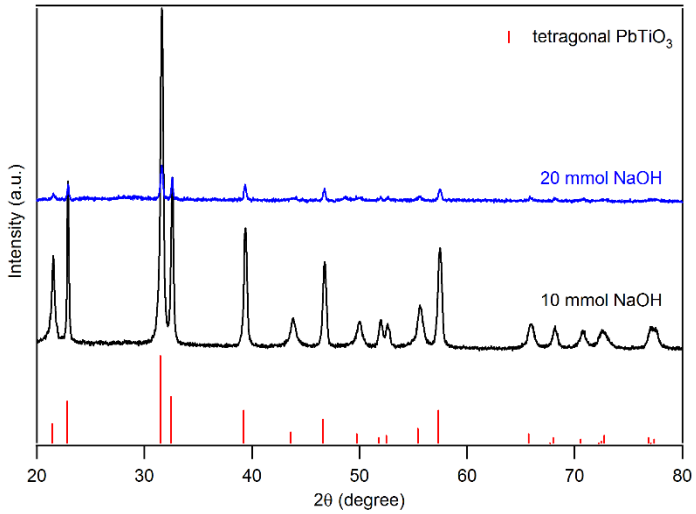

Figure 5-8: XRD patterns of samples synthesized with 10 mmol (black) and 20 mmol (blue) NaOH. The red vertical line at the bottom represents XRD pattern of bulk tetragonal $PbTiO_3$.

Figure 5-9 (a) shows an SEM image of a sample synthesized with 10 mmol NaOH. Wire-like nanostructures can be easily observed on the surface of big chunks in the higher magnification SEM image (Figure 5-9 (a) inset). With 20 mmol NaOH, the obtained sample has a nanoribbon-like shape as shown in Figure 5-9 (b). Figure 5-9 (c) shows a TEM image of a sample synthesized

with 20 mmol NaOH. Thin nanoribbons can be observed in the overview image which are consistent with the low peak intensity of the corresponding XRD pattern. The HRTEM image of a single nanoribbon (Figure5-9 (c) Inset) shows the nanostructure is crystalline with lattice spacing of ca. 3.83 Å which is close to the reported value of 3.90 Å of $PbTiO_3$ (100)[121].

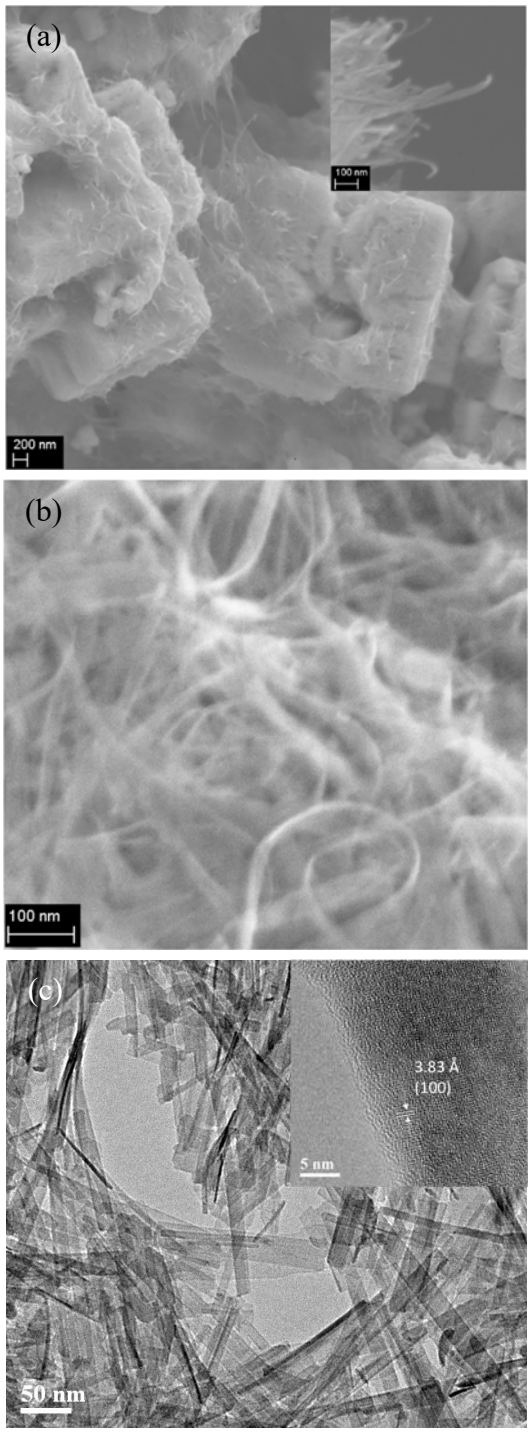

Figure 5-9: Low (a) and high (inset) magnification SEM images of the samples synthesized with 10 mmol NaOH. SEM (b) and TEM (c) images of the sample synthesized with 20 mmol NaOH. (c) Inset: HRTEM image of a single nanoribbon.

Chapter 6 Conclusions and Future Work

6.1 Mn-doped $BaTiO_3$

As a part of this thesis I performed a study on the influence of solvents and doping concentrations on the growth of Mn-doped $BaTiO_3$ NCs. Crystal structure and morphology of the synthesized NCs were investigated using XRD, Raman spectroscopy and TEM. 10% Mn-doped $BaTiO_3$ samples were prepared in water, ethanol and benzyl alcohol. Water-synthesized quasi-spherical NPs with average sizes above 100 nm have tetragonal crystal structure. EDX line scans of the single nanostructure reveals a hollow structure which suggests that these NPs are likely formed by oriented attachment of small NCs. NCs prepared in ethanol and benzyl alcohol have an average size of ca. 6.2 nm and 4.0 nm, respectively. Ethanol-synthesized NCs maintain some tetragonality which is likely related to a local distortion. The samples synthesized in benzyl alcohol have predominantly a cubic perovskite structure. The presence of dopant ions in $BaTiO_3$ NCs synthesized in ethanol favors the phase transformation form tetragonal to cubic structure as indicated by the Raman spectra of Mn-doped $BaTiO_3$ with different Mn concentration. The ligand field transition of Mn^{3+} ions in distorted octahedral sites was observed in UV-visible absorption spectra, suggesting the presence of a small amount of Mn^{3+} ions in the sample, which agrees well with the analysis of the Mn L-edge X-ray absorption spectrum.

Electrostatic force microscopy (EFM) measurements of the individual NPs will provide direct evidence of the ferroelectric properties of Mn-doped $BaTiO_3$ NPs. From the magnetic-field dependence of EFM measurements, the ME coupling in Mn-doped $BaTiO_3$ can be extracted. The coexistence of Mn^{2+} and Mn^{3+} ions will enable us to examine different possible mechanisms of long range magnetic ordering in transition-metal ions doped ferroelectrics, such as defect-mediated exchange interactions and charge-transfer ferromagnetism. Furthermore, comparing the magnetic

and electric properties of Mn-doped $BaTiO_3$ with that of Cr-doped $BaTiO_3$ could shed light on the influence of d-occupancy of magnetic dopants on the $BaTiO_3$ phase transformation and magnetic ordering in the ferroelectric lattice.

6.2 $Co_{0.6}Fe_{2.4}O_4$-$BaTiO_3$ Composite

$BaTiO_3$ building blocks (BTO1 and BTO2) with different sizes were synthesized and combined with $Co_{0.6}Fe_{2.4}O_4$ nanocubes (CFO) using an impregnation and spin coating method. BTO1 with a larger size has a tetragonal perovskite structure. BTO2 aggregates are formed by the oriented attachment of small NPs as confirmed by TEM investigations. The formation of large domains helps stabilize the tetragonal phase in BTO2. CFO samples with cube-like morphology have an average size of ca. 22.5 nm. Both XRD and Raman spectroscopy measurements confirmed that the synthesized CFO sample has the same inverse spinel structure as $CoFe_2O_4$. As-synthesized sample exhibits a magnetic hysteresis loop at room temperature with coercivity of ca. 1400 Oe and saturation magnetization of ca. 50 emu/g. The crystal structure of BTO1 and BTO2 does not change after a mild annealing process during sample preparation. The CFO-BTO2 composite has a higher loading of CFO building blocks compared to the CFO-BTO1 composite as indicated by XRD and Raman spectroscopy. Magnetic properties of the composites are similar to those of CFO component with slightly higher coercivity which is attributed to the elimination of oxygen defects during the annealing process.

So far, the ferroelectric properties of both $BaTiO_3$ and the composites are indicated by the tetragonality of the crystal structure determined mainly by XRD and Raman. The electrical measurements will enable us to quantitatively understand the ferroelectric properties of the samples. With the presence of an external magnetic field, the electric measurement can also be used to examine ME coupling between the two building blocks. Furthermore, XMCD studies on

Ti L-edge in addition to Fe/Co L-edge can be very helpful to understand the mechanism of ME coupling. The correlation between the two spectra (including sign and magnitude of the XMCD signal) will allow us to unambiguously demonstrate the possibility of inducing magnetization into a ferroelectric component, as the first step toward truly multiferroic nanostructures. Using STXM, the XMCD spectra with high spatial resolution can help understand the magnetization of ferroelectric component, and particularly the role of NCs interfaces.

6.3 $Co_{0.6}Fe_{2.4}O_4$-$PbTiO_3$ Composite

$PbTiO_3$ thin films were obtained by annealing spin-coated thin films made of amorphous NPs. Both XRD and Raman spectroscopy results confirm the tetragonal perovskite crystal structure of the annealed thin film. The UV-visible absorption spectrum of a $PbTiO_3$ thin film reveals band gap energy of ca. 3.4 eV. The absorption spectra of $Co_{0.6}Fe_{2.4}O_4$-$PbTiO_3$ multilayer thin films comprise both $PbTiO_3$ and $Co_{0.6}Fe_{2.4}O_4$ nanostructures which provides an opportunity to monitor the behavior of both components under an external magnetic field using MCD measurements. In addition, the interface between $PbTiO_3$ and $Co_{0.6}Fe_{2.4}O_4$ domains in the composite are clearly observed in HRTEM images. This allows us to address the interfacial effect of ME coupling by XMCD measurements in STXM mode.

The transparency together with more robust ferroelectricity serves as an excellent opportunity for the spectroscopic studies and fabrication of opto-electrical devices. In multiferroics, the coupling between the electric and magnetic states leads to different magnetoelectric effect. The transparent multiferroic thin films provide the opportunity to investigate the optical properties of the multiferroics under electric and magnetic field in the visible light range which might open a new horizon in photonics.

Appendix

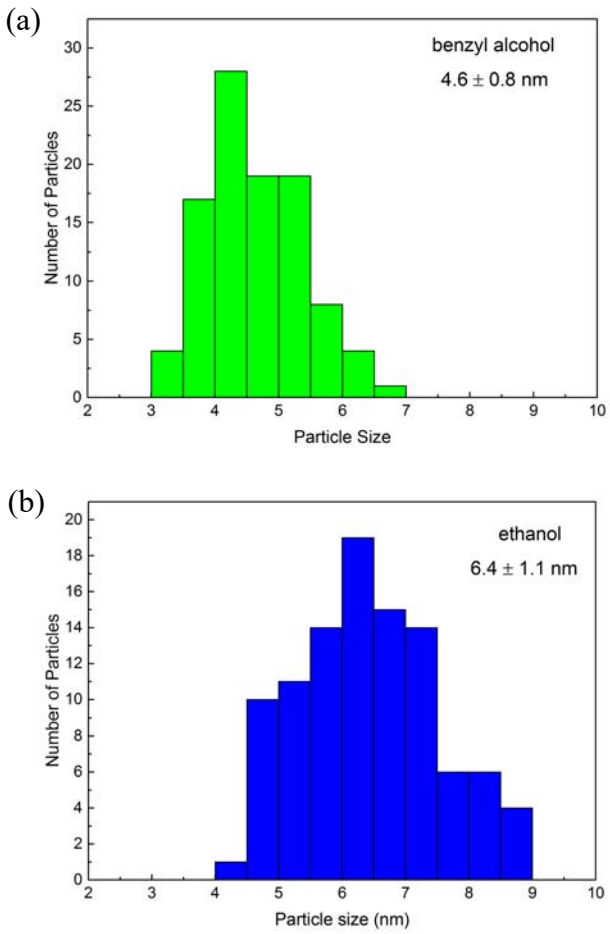

Figure A1: Particle size histogram of 10% Mn-doped $BaTiO_3$ synthesized in benzyl alcohol (a) and ethanol (b).

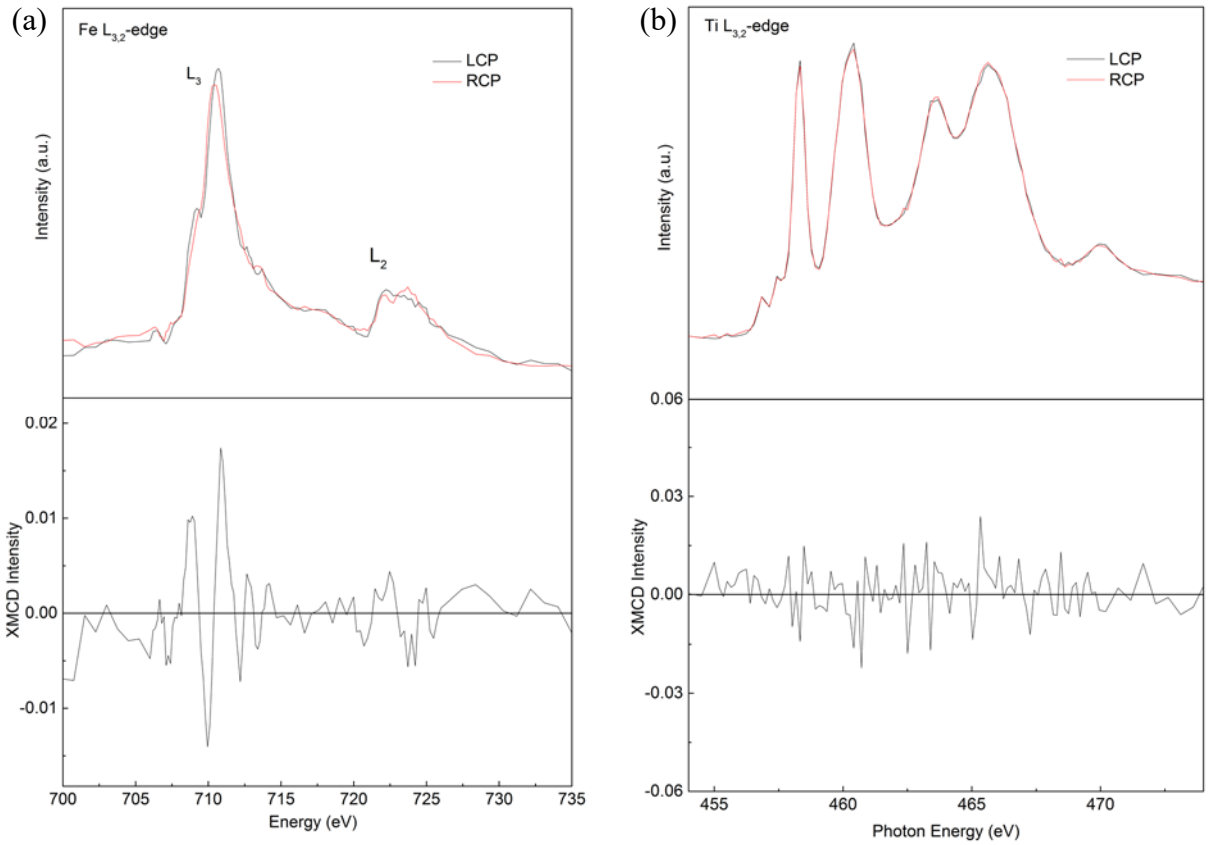

Figure A2: Fe (a) and Ti (b) $L_{3,2}$-edge XANES (top) and XMCD (bottom) in composite of $CoFe_2O_4$ and $BaTiO_3$.

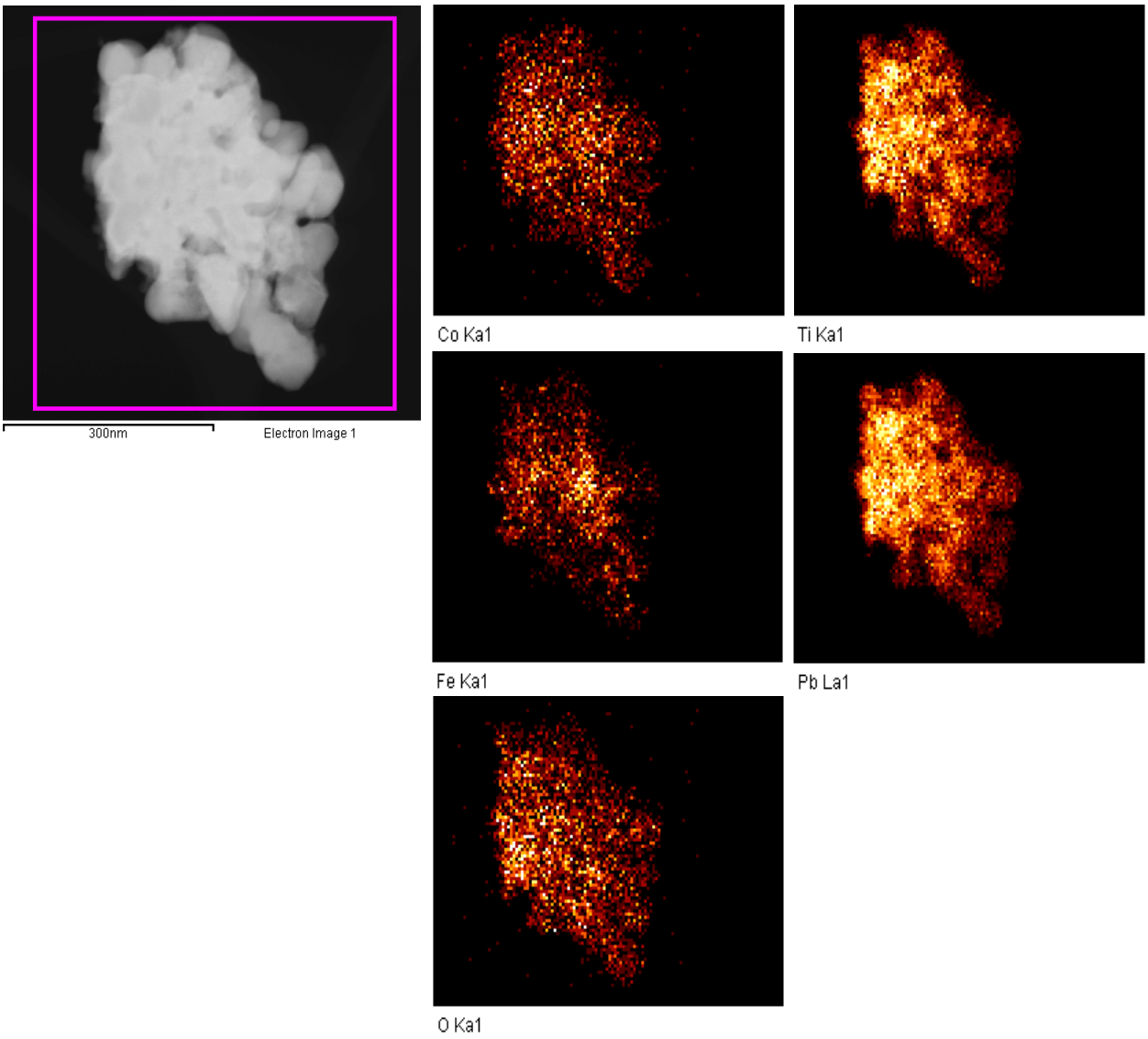

Figure A3: STEM image of the fragment of CFO-PTO thin film with corresponding EDX elemental maps of Co, Fe, Pb, Ti, and O in STEM.

References

(1) Devonshire, A. F. *Adv. Phys.* **1954**, *3* (10), 85–130.

(2) Zhong, W.; Vanderbilt, D.; Rabe, K. M. *Phys. Rev. Lett.* **1994**, *73* (13), 1861–1864.

(3) Valasek, J. *Phys. Rev.* **1921**, *17* (4), 475–481.

(4) Blinc, R. Order and Disorder in Perovskites and Relaxor Ferroelectrics. In *Structure and Bonding*; Dalal, N., Bussmann-Holder, A., Eds.; Springer: Berlin, Heidelberg, 2007; Vol. 124, pp 51-67.

(5) Ju, L.; Sabergharesou, T.; Stamplecoskie, K. G.; Hegde, M.; Wang, T.; Combe, N. a; Wu, H.; Radovanovic, P. V. *J. Am. Chem. Soc.* **2012**, *134* (2), 1136–1146.

(6) Wu, Z.; Cohen, R. E. *Phys. Rev. Lett.* **2005**, *95* (3), 1–4.

(7) Hill, N. a. *J. Phys. Chem. B* **2000**, *104* (29), 6694–6709.

(8) Cohen, R. E. *Nature* **1992**, *358* (6382), 136–138.

(9) Piskunov, S.; Kotomin, E. a.; Heifets, E.; Maier, J.; Eglitis, R. I.; Borstel, G. *Surf. Sci.* **2005**, *575* (1), 75–88.

(10) Wang, J. J.; Meng, F. Y.; Ma, X. Q.; Xu, M. X.; Chen, L. Q. *J. Appl. Phys.* **2010**, *108* (3), 034107.

(11) Iijima, K.; Tomita, Y.; Takayama, R.; Ueda, I. *J. Appl. Phys.* **1986**, *60* (1), 361–367.

(12) Cohen, R. E. *J. Phys. Chem. Solids* **2000**, *61* (2), 139–146.

(13) Shirane, G.; Frazer, B. C.; Minkiewicz, V. J.; Leake, J. a.; Linz, a. *Phys. Rev. Lett.* **1967**, *19* (5), 234–235.

(14) Uchino, K.; Sadanaga, E.; Hirose, T. *J. Am. Ceram. Soc.* **1989**, *72* (8), 1555–1558.

(15) Yashima, M.; Hoshina, T.; Ishimura, D.; Kobayashi, S.; Nakamura, W.; Tsurumi, T.; Wada,

S. *J. Appl. Phys.* **2005**, *98* (1), 014313.

(16) Spanier, J. E.; Kolpak, A. M.; Urban, J. J.; Grinberg, I.; Ouyang, L.; Yun, W. S.; Rappe, A. M.; Park, H. *Nano Lett.* **2006**, *6* (4), 735–739.

(17) Li, X.; Shih, W. *J. Am. Ceram. Soc.* **1997**, *80* (11), 2844–2852.

(18) Mara, R.; Sutherland, G.; Tyrell, H. *Phys. Rev.* **1954**, *96* (3), 801–802.

(19) Adireddy, S.; Lin, C.; Cao, B.; Zhou, W.; Caruntu, G. *Chem. Mater.* **2010**, *22* (6), 1946–1948.

(20) Polking, M. J.; Han, M.-G.; Yourdkhani, A.; Petkov, V.; Kisielowski, C. F.; Volkov, V. V; Zhu, Y.; Caruntu, G.; Alivisatos, a P.; Ramesh, R. *Nat. Mater.* **2012**, *11* (8), 700–709.

(21) Jiang, B.; Peng, J. L.; Bursill, L. a.; Zhong, W. L. *J. Appl. Phys.* **2000**, *87* (7), 3462–3467.

(22) Ishikawa, K.; Yoshikawa, K.; Okada, N. *Phys. Rev. B* **1988**, *37* (10), 5852–5855.

(23) Zhong, W. L.; Jiang, B.; Zhang, P. L.; Ma, J. M.; Cheng, H. M.; Yang, Z. H. *J. Phys. Condens. Matter* **1993**, *5* (16), 2619–2624.

(24) De Keijser, M.; Dormans, G. J. M.; Van Veldhoven, P. J.; De Leeuw, D. M. *Appl. Phys. Lett.* **1991**, *59* (27), 3556–3558.

(25) Zhong, W.; Wang, Y.; Zhang, P.; Qu, B. *Phys. Rev. B* **1994**, *50* (2), 698–703.

(26) Chen, Y. F.; Yu, T.; Chen, J.; Shun, L.; Li, P.; Ming, N. *Appl. Phys. Lett.* **1995**, *66* (2), 148–150.

(27) Stefanita, C.-G. *Magnetism*; Springer: Berlin, Heidelberg, 2012; pp1-28.

(28) Cullity, B. D.; Graham, C. D. *Introduction to Magnetic Materials*, 2nd ed.; Wiley-IEEE Press: Hoboken, New Jersey, 2008; pp 275-329..

(29) Zapperi, S.; Cizeau, P.; Durin, G.; Stanley, H. E. *Phys. Rev. B* **1998**, *58* (10), 6353–6366.

(30) Wang, Z. L. *Characterization of Nanophase Materials*; WILEY–VCH Verlag GmbH: Weinheim, Germany, 2001; pp 289-314.

(31) White, R. M. *Quantum Theory of Magnetism*; Springer: Berlin, Heidelberg, 1983; pp 44-52.

(32) Kittel, C. *Rev. Mod. Phys.* **1949**, *21* (4), 541–583.

(33) Arenholz, E.; van der Laan, G.; Chopdekar, R. V.; Suzuki, Y. *Phys. Rev. B* **2006**, *74* (9), 094407.

(34) Pannaparayil, T.; Marande, R.; Komarneni, S.; Sankar, S. G. *J. Appl. Phys.* **1988**, *64* (10), 5641–5643.

(35) Coey, J. M. D. *Magnetism and Magnetic Materials*; Cambridge University Press: Cambridge, 2010; pp 195-220.

(36) Szotek, Z.; Temmerman, W. M.; Ködderitzsch, D.; Svane, A.; Petit, L.; Winter, H. *Phys. Rev. B* **2006**, *74* (17), 174431.

(37) Stoner, E. C.; Wohlfarth, E. P. *Philos. Trans. R. Soc. London. Ser. A. Math. Phys. Sci.* **1948**, *240* (826), 599–642.

(38) Song, Q.; Zhang, Z. J. *J. Am. Chem. Soc.* **2004**, *126* (19), 6164–6168.

(39) Li, X.-H.; Xu, C.-L.; Han, X.-H.; Qiao, L.; Wang, T.; Li, F.-S. *Nanoscale Res. Lett.* **2010**, *5* (6), 1039–1044.

(40) Yu, Y.; Mendoza-Garcia, A.; Ning, B.; Sun, S. *Adv. Mater.* **2013**, *25* (22), 3090–3094.

(41) Schmid, H. *Ferroelectrics* **1994**, *162* (1), 317–338.

(42) Spaldin, N. A.; Cheong, S.; Ramesh, R. *Phys. Today* **2010**, *63* (10), 38–43.

(43) Zhai, J.; Xing, Z.; Dong, S.; Li, J.; Viehland, D. *Appl. Phys. Lett.* **2006**, *88* (6), 3–6.

(44) Liu, M.; Obi, O.; Lou, J.; Chen, Y.; Cai, Z.; Stoute, S.; Espanol, M.; Lew, M.; Situ, X.; Ziemer, K. S.; Harris, V. G.; Sun, N. X. *Adv. Funct. Mater.* **2009**, *19* (11), 1826–1831.

(45) Dong, S.; Li, J. F.; Viehland, D.; Cheng, J.; Cross, L. E. *Appl. Phys. Lett.* **2004**, *85* (16), 3534–3536.

(46) Gajek, M.; Bibes, M.; Fusil, S.; Bouzehouane, K.; Fontcuberta, J.; Barthélémy, A.; Fert, A. *Nat. Mater.* **2007**, *6* (4), 296–302.

(47) Fiebig, M. *J. Phys. D. Appl. Phys.* **2005**, *38* (8), R123–R152.

(48) Khomskii, D. *Physics (College. Park. Md).* **2009**, *2*, 20.

(49) Wang, J.; Neaton, J. B.; Zheng, H.; Nagarajan, V.; Ogale, S. B.; Liu, B.; Viehland, D.; Vaithyanathan, V.; Schlom, D. G.; Waghmare, U. V; Spaldin, N. a; Rabe, K. M.; Wuttig, M.; Ramesh, R. *Science* **2003**, *299* (5613), 1719–1722.

(50) Kimura, T.; Goto, T.; Shintani, H.; Ishizaka, K.; Arima, T.; Tokura, Y. *Nature* **2003**, *426* (6), 55–58.

(51) Ravindran, P.; Vidya, R.; Kjekshus, A.; Fjellvåg, H.; Eriksson, O. *Phys. Rev. B* **2006**, *74* (22), 224412.

(52) Ederer, C.; Spaldin, N. a. *Phys. Rev. B* **2006**, *74* (2), 020401.

(53) Archer, P. I.; Radovanovic, P. V.; Heald, S. M.; Gamelin, D. R. *J. Am. Chem. Soc.* **2005**, *127* (41), 14479–14487.

(54) Schwartz, D. a; Norberg, N. S.; Nguyen, Q. P.; Parker, J. M.; Gamelin, D. R. *J. Am. Chem. Soc.* **2003**, *125* (43), 13205–13218.

(55) Radovanovic, P. V; Gamelin, D. R. *Phys. Rev. Lett.* **2003**, *91* (15), 157202.

(56) Son, J. Y.; Lee, J. H.; Song, S.; Shin, Y. H.; Jang, H. M. *ACS Nano* **2013**, *7* (6), 5522–5529.

(57) Verma, K. C.; Kotnala, R. K.; Negi, N. S. *Appl. Phys. Lett.* **2008**, *92* (15), 152902.

(58) Apostolova, I. N.; Apostolov, a. T.; Golrokh Bahoosh, S.; Wesselinowa, J. M. *J. Appl. Phys.* **2013**, *113* (20), 203904.

(59) Coey, J. M. D.; Venkatesan, M.; Fitzgerald, C. B. *Nat. Mater.* **2005**, *4* (2), 173–179.

(60) Coey, J. M. D.; Wongsaprom, K.; Alaria, J.; Venkatesan, M. *J. Phys. D. Appl. Phys.* **2008**, *41* (13), 134012.

(61) Farvid, S. S.; Sabergharesou, T.; Hutfluss, L. N.; Hegde, M.; Prouzet, E.; Radovanovic, P. V. *J. Am. Chem. Soc.* **2014**, *136* (21), 7669–7679.

(62) Van Suchtelen J. *Philips Res. Rep* **1972**, *27* (1), 28–37.

(63) Zheng, H.; Wang, J.; Lofland, S. E.; Ma, Z.; Mohaddes-Ardabili, L.; Zhao, T.; Salamanca-Riba, L.; Shinde, S. R.; Ogale, S. B.; Bai, F.; Viehland, D.; Jia, Y.; Schlom, D. G.; Wuttig, M.; Roytburd, a; Ramesh, R. *Science* **2004**, *303* (5658), 661–663.

(64) Duong, G. V; Groessinger, R.; Turtelli, R. S. *IEEE Trans. Magn.* **2006**, *42* (10), 3611–3613.

(65) Corral-Flores, V.; Bueno-Baques, D.; Carrillo-Flores, D.; Matutes-Aquino, J. A. *J. Appl. Phys.* **2006**, *99* (8), 08J503.

(66) Raidongia, K.; Nag, A.; Sundaresan, A.; Rao, C. N. R. *Appl. Phys. Lett.* **2010**, *97* (6), 062904.

(67) Corral-Flores, V.; Bueno-Baqués, D.; Ziolo, R. F. *Acta Mater.* **2010**, *58* (3), 764–769.

(68) Duan, C.-G.; Jaswal, S.; Tsymbal, E. *Phys. Rev. Lett.* **2006**, *97* (4), 047201.

(69) Kim, D.; Lee, H.; Kim, G.; Koo, Y.; Jung, J.; Shin, H.; Kim, J.-Y.; Kang, J.-S. *Phys. Rev. B* **2009**, *79* (3), 033402.

(70) Valencia, S.; Crassous, a; Bocher, L.; Garcia, V.; Moya, X.; Cherifi, R. O.; Deranlot, C.; Bouzehouane, K.; Fusil, S.; Zobelli, a; Gloter, a; Mathur, N. D.; Gaupp, a; Abrudan, R.; Radu, F.; Barthélémy, a; Bibes, M. *Nat. Mater.* **2011**, *10* (10), 753–758.

(71) Schmitz-Antoniak, C.; Schmitz, D.; Borisov, P.; de Groot, F. M. F.; Stienen, S.; Warland, A.; Krumme, B.; Feyerherm, R.; Dudzik, E.; Kleemann, W.; Wende, H. *Nat. Commun.* **2013**, *4*, 2051.

(72) Hu, Y.; Gu, H.; Sun, X.; You, J.; Wang, J. *Appl. Phys. Lett.* **2006**, *88* (19), 193120.

(73) Sathyanarayana, D. N. *Electronic Absorption Spectroscopy and Related Techniques*; Univerisities Press (India) Limited: Hyderabad, 2001; pp 98-106.

(74) Ferraro, J. R.; Nakamoto, K.; Brown, C. W. *Introductory Raman Spectroscopy*, 2nd ed.; Elsevier, 2003; pp 10-40.

(75) Smith, M. B.; Page, K.; Siegrist, T.; Redmond, P. L.; Walter, E. C.; Seshadri, R.; Brus, L. E.; Steigerwald, M. L. *J. Am. Chem. Soc.* **2008**, *130* (22), 6955–6963.

(76) Cerdeira, F., Holzapfel, W. B., Bauerle, D. *Phys. Rev. B* **1975**, *11* (3), 1188–1192.

(77) Bunker, G. Introduction to XAFS. *A Practical Guide to X-ray Absorption Fine Structure Spectroscopy*, Cambridge University Press: Cambridge, 2010; pp 80-105.

(78) Söderlind, P.; Eriksson, O.; Johansson, B.; Albers, R. C.; Boring, A. M. *Phys. Rev. B* **1992**, *45* (22), 12911–12916.

(79) Carra, P.; Thole, B. T.; Altarelli, M.; Wang, X. *Phys. Rev. Lett.* **1993**, *70* (5), 694–697.

(80) Shiratori, Y.; Pithan, C.; Dornseiffer, J.; Waser, R. *J. Raman Spectrosc.* **2007**, *38* (10), 1288–1299.

(81) Wei, X.; Xu, G.; Ren, Z.; Wang, Y.; Shen, G.; Han, G. *J. Am. Ceram. Soc.* **2007**, *91* (1), 315–318.

(82) Liu, Z.; Sun, D. D.; Guo, P.; Leckie, J. O. *Chem. - A Eur. J.* **2007**, *13* (6), 1851–1855.

(83) Pradhan, D.; Leung, K. T. *J. Mater. Chem.* **2009**, *19* (28), 4902–4905.

(84) Zhu, J.; Ng, K. Y. S.; Deng, D. *ACS Appl. Mater. Interfaces* **2014**, *6* (4), 2996–3001.

(85) Sun, Z.; Xie, K.; Li, Z. A.; Sinev, I.; Ebbinghaus, P.; Erbe, A.; Farle, M.; Schuhmann, W.; Muhler, M.; Ventosa, E. *Chem. - A Eur. J.* **2014**, *20* (7), 2022–2030.

(86) Fan, H. J.; Scholz, R.; Kolb, F. M.; Zacharias, M.; Gösele, U. *Solid State Commun.* **2004**, *130* (8), 517–521.

(87) DiDomenico, M.; Wemple, S. H.; Porto, S. P. S.; Bauman, R. P. *Phys. Rev.* **1968**, *174* (2), 522–530.

(88) Suzuki, K.; Kijima, K. *Jpn. J. Appl. Phys.* **2005**, *44* (4A), 2081–2082.

(89) Sabergharesou, T.; Wang, T.; Ju, L.; Radovanovic, P. V. *Appl. Phys. Lett.* **2013**, *103* (1), 012401.

(90) Lever, A. B. P. *Inorganic Electronic Spectroscopy*, 2nd ed.; Elsevier: Amsterdam, 1984; pp 240-290.

(91) Smith, G.; Hålenius, U.; Langer, K. *Phys. Chem. Miner.* **1982**, *8* (3), 136–142.

(92) Abs-Wurmbach, I., Langer, K., Tillmanns, E. *Naturwissenschaften* **1977**, *64*, 527–528.

(93) Stavitski, E.; de Groot, F. M. F. *Micron* **2010**, *41* (7), 687–694.

(94) Groot, F. de. *Coord. Chem. Rev.* **2005**, *249* (1-2), 31–63.

(95) Garvie, L. a. J.; Craven, a. J. *Phys. Chem. Miner.* **1994**, *21* (4), 191–206.

(96) Kolen'ko, Y. V.; Kovnir, K. a.; Neira, I. S.; Taniguchi, T.; Ishigaki, T.; Watanabe, T.; Sakamoto, N.; Yoshimura, M. *J. Phys. Chem. C* **2007**, *111* (20), 7306–7318.

(97) Kalyani, V.; Vasile, B. S.; Ianculescu, A.; Testino, A.; Carino, A.; Buscaglia, M. T.; Buscaglia, V.; Nanni, P. *Cryst. Growth Des.* **2015**, acs.cgd.5b00770.

(98) Zhang, Y.; Or, S. W.; Wang, X.; Cui, T.; Cui, W.; Zhang, Y.; Zhang, Z. *Eur. J. Inorg. Chem.* **2009**, *2009* (1), 168–173.

(99) R. LEE PENN and Banfield, J. F. *Am. Mineral.* **1998**, *83* (9-10), 1077–1082.

(100) Wu, L.; Jubert, P.-O.; Berman, D.; Imaino, W.; Nelson, A.; Zhu, H.; Zhang, S.; Sun, S. *Nano Lett.* **2014**, *14* (6), 3395–3399.

(101) Park, M. H.; Lee, Y. H.; Kim, H. J.; Kim, Y. J.; Moon, T.; Kim, K. Do; Müller, J.; Kersch, A.; Schroeder, U.; Mikolajick, T.; Hwang, C. S. *Adv. Mater.* **2015**, *27* (11), 1811–1831.

(102) Shemer, G.; Tirosh, E.; Livneh, T.; Markovich, G. *J. Phys. Chem. C* **2007**, *111* (39), 14334–14338.

(103) Wang, Z.; Downs, R. T.; Pischedda, V.; Shetty, R.; Saxena, S. K.; Zha, C. S.; Zhao, Y. S.; Schiferl, D.; Waskowska, A. *Phys. Rev. B* **2003**, *68* (9), 094101.

(104) Chandramohan, P.; Srinivasan, M. P.; Velmurugan, S.; Narasimhan, S. V. *J. Solid State Chem.* **2011**, *184* (1), 89–96.

(105) Pappalardo, R.; Wood, D. L.; Linares, R. C. *J. Chem. Phys.* **1961**, *35* (6), 2041–2059.

(106) Tirosh, E.; Shemer, G.; Markovich, G. *Chem. Mater.* **2006**, *18* (2), 465–470.

(107) Fontijn, W. F. J.; van der Zaag, P. J.; Feiner, L. F.; Metselaar, R.; Devillers, M. a. C. *J. Appl. Phys.* **1999**, *85* (8), 5100–5105.

(108) Kim, K. J.; Lee, H. S.; Lee, M. H.; Lee, S. H. *J. Appl. Phys.* **2002**, *91* (12), 9974–9977.

(109) Fontijn, W. F. J.; van der Zaag, P. J.; Metselaar, R. *J. Appl. Phys.* **1998**, *83* (11), 6765–6767.

(110) Bersani, D.; Montenero, A.; Pigoni, S.; Gnappi, G. *J. Non. Cryst. Solids* **1995**, *193*, 490–493.

(111) Yao, K.; Zhang, L.; Yao, X.; Zhu, W. *Mater. Sci. Eng. B* **1996**, *41* (3), 322–328.

(112) Camargo, E. R.; Longo, E.; Leite, E. R.; Mastelaro, V. R. *J. Solid State Chem.* **2004**, *177* (6), 1994–2001.

(113) Burns, G.; Scott, B. a. *Phys. Rev. Lett.* **1970**, *25* (3), 167–170.

(114) Burns, G.; Scott, B. a. *Phys. Rev. B* **1973**, *7* (7), 3088–3101.

(115) Fontana, M. D.; Idrissi, H.; Kugel, G. E.; Wojcik, K. *J. Phys. Condens. Matter* **1991**, *3* (44), 8695–8705.

(116) Fu, D. S.; Iwazaki, H.; Suzuki, H.; Ishikawa, K. *J. Phys. Condens. Matter* **2000**, *12* (4), 399–414.

(117) Wang, J.; Wylie-van Eerd, B.; Sluka, T.; Sandu, C.; Cantoni, M.; Wei, X.; Kvasov, A.; McGilly, L. J.; Gemeiner, P.; Dkhil, B.; Tagantsev, A.; Trodahl, J.; Setter, N. *Nat. Mater.* **2015**, *14* (10), 985–990.

(118) Peng, C. H.; Chang, J.-F.; Desu, S. B. *MRS Proc.* **1991**, *243*, 21.

(119) Moret, M. P.; Devillers, M. a C.; Wörhoff, K.; Larsen, P. K. *J. Appl. Phys.* **2002**, *92* (1), 468–474.

(120) Riman, R., Suchanek, W., Lencka, M. *Ann. Chim. Sci. des Matériaux* **2002**, *27* (6), 15–36.

(121) Xu, G.; Huang, X.; Krstic, V.; Chen, S.; Yang, X.; Chao, C.; Shen, G.; Han, G. *CrystEngComm* **2014**, *16* (21), 4373–4376.